

## **Hepatic Rab24 controls blood glucose homeostasis via improving mitochondrial plasticity**

Susanne Seitz<sup>1,2</sup>, Yun Kwon<sup>1,2</sup>, Goetz Hartleben<sup>1,2</sup>, Julia Jülg<sup>3</sup>, Revathi Sekar<sup>1,2</sup>, Natalie Krahmer<sup>4,7</sup>, Bahar Najafi<sup>1,2</sup>, Anne Loft<sup>1,2</sup>, Sofiya Gancheva<sup>5,6,2</sup>, Kerstin Stemmer<sup>7,2</sup>, Annette Feuchtinger<sup>8</sup>, Martin Hrabe de Angelis<sup>9,10,2</sup>, Timo D. Müller<sup>7,2,11</sup>, Matthias Mann<sup>4,12</sup>, Matthias Blüher<sup>13</sup>, Michael Roden<sup>5,6,2</sup>, Mauricio Berriel Diaz<sup>1,2</sup>, Christian Behrends<sup>3</sup>, Jerome Gilleron<sup>14</sup>, Stephan Herzig<sup>1,2</sup> and Anja Zeigerer<sup>1,2,\*</sup>

1. Institute for Diabetes and Cancer, Helmholtz Center Munich, 85764 Neuherberg, Germany, Joint Heidelberg-IDC Translational Diabetes Program, Inner Medicine 1, Heidelberg University Hospital, Heidelberg, Germany, and Chair Molecular Metabolic Control, Technical University Munich, Germany

2. German Center for Diabetes Research (DZD), 85764 Neuherberg, Germany

3. Munich Cluster for Systems Neurology, Ludwig-Maximilians-University München, 81377 Munich, Germany

4. Proteomics and Signal Transduction, Max-Planck Institute of Biochemistry, 82152 Martinsried, Germany

5. Division of Endocrinology and Diabetology, Medical Faculty, Heinrich Heine University, Düsseldorf, Germany

6. Institute for Clinical Diabetology, German Diabetes Center, Leibniz Center for Diabetes Research at Heinrich Heine University, Dusseldorf, Germany

7. Institute for Diabetes and Obesity, Helmholtz Center Munich, 85764 Neuherberg, Germany

8. Research Unit Analytical Pathology, Helmholtz Center Munich, 85764 Neuherberg, Germany

9. Institute of Experimental Genetics, Helmholtz Zentrum München, German Research Center for Environmental Health, Ingolstädter Landstrasse 1, 85764 Neuherberg, Germany

10. Chair of Experimental Genetics, School of Life Science Weihenstephan, Technische Universität München, Alte Akademie 8, 85354 Freising, Germany

11. Department of Pharmacology and Experimental Therapy, Institute of Experimental and Clinical Pharmacology and Toxicology, Eberhard Karls University Hospitals and Clinics, Tübingen, Germany.

12. NF Center for Protein Research, Faculty of Health Sciences, University of Copenhagen, 2200 Copenhagen, Denmark

13. Department of Medicine, University of Leipzig, 04103 Leipzig, Germany

14. Université Côte d'Azur, Institut National de la Santé et de la Recherche Médicale (Inserm) UMR1065, Mediterranean Center of Molecular Medicine C3M, France

\* Correspondence: Anja Zeigerer (anja.zeigerer@helmholtz-muenchen.de)

## **SUMMARY**

Non-alcoholic fatty liver disease (NAFLD) represents a key feature of obesity related type-2 diabetes with increasing prevalence worldwide. No treatment options are available to date, paving the way to more severe liver damage, including cirrhosis and hepatocellular carcinoma. Here, we show an unexpected function for an intracellular trafficking regulator, the small Rab GTPase Rab24, in mitochondrial fission and activation with immediate impact on hepatic and systemic energy homeostasis. RAB24 is highly upregulated in livers of obese NAFLD patients and positively correlates with increased body fat in humans. Liver-selective inhibition of Rab24 increases autophagic flux and mitochondrial connectivity leading to a strong improvement in hepatic steatosis and a reduction in serum glucose and cholesterol levels in obese mice. Our study highlights a potential therapeutic application of trafficking regulators, such as Rab24, for NAFLD, and establishes a conceptual functional connection between intracellular transport and systemic metabolic dysfunction.

## INTRODUCTION

Intracellular transport controls the internalization of nutrients into cells, the fine-tuning and downregulation of signaling receptors and the packaging and secretion of proteins, lipids and other metabolites<sup>1-6</sup>. These functions are mediated via vesicular trafficking, which is controlled by coat proteins, SNAREs and Rab GTPases that collectively enable the specificity in the intracellular distribution of cargoes<sup>4,6-9</sup>. This trafficking network is sensitive to extracellular cues and alters its kinetics and fates of transport depending on different environmental stimuli, including metabolic challenges<sup>10</sup>. Controlling the internalization of nutrient transporters and activated signaling receptors as well as the secretion of metabolically active proteins places this system theoretically into central stage of metabolic control. Surprisingly, although this connection seems obvious, the tight link between metabolite channeling and intracellular trafficking is still mainly unexplored<sup>6</sup>. Hundreds of trafficking components are involved in intracellular transport, providing a large population of potential metabolic regulators waiting to be characterized.

Here, we present Rab24, which was originally described in the late endosomal pathway<sup>11,12</sup>, as a regulator in the mitochondrial fusion/fission cycle through direct interaction with the Fission protein 1 (FIS1). Reduction of Rab24 reduces mitochondrial fission, resulting in elongated and more connected mitochondria and increases mitochondrial respiration. As Rab24 knockdown (KD) in wild type, high fat diet (HFD) and methionine-choline deficient-HFD (MCD-HFD)-treated mice strongly improves glucose homeostasis and liver steatosis, our data emphasizes a unknown role of Rab24 in metabolic control.

## RESULTS

### Rab24 is highly upregulated in patients with fatty liver

To identify trafficking candidates with functional impact on metabolic control, we screened over 1200 knockout mice for their glucose sensitivity using an oral glucose tolerance test (OGTT)<sup>13</sup>. Out of five trafficking regulators with alteration (+/-15%) in systemic glucose clearance, whole body knockout of Rab24 led to the most robust improvement in glucose tolerance, supporting a critical regulatory function of Rab24 in systemic glucose homeostasis. To ensure that Rab24 is also necessary for human metabolic control, we studied its abundance in two independent cohorts of patients with metabolic diseases. Alterations in liver metabolism are known to affect systemic glucose homeostasis and are associated with obesity-related type 2 diabetes<sup>14,15</sup>. Thus, we first tested hepatic *RAB24* expression in a cohort of obese patients versus healthy controls. Interestingly, *RAB24* was 3-fold upregulated in the liver of obese patients (**Fig. 1a**). This was associated with a positive correlation of Rab24 with BMI and a negative correlation with the Clamp GIR (**Extended Data Fig. 1a, b**) across the entire patient cohort. In addition, we observed a positive correlation with visceral fat ( $r=0.375$ ,  $p=0.02$ ), liver fat ( $r=0.346$ ,  $p=0.03$ ), HDL-cholesterol levels ( $r=0.367$ ,  $p=0.02$ ), free fatty acids ( $r=0.34$ ,  $p=0.03$ ) and leptin ( $r=0.46$ ,  $p=0.005$ ) levels in these patients, overall indicating that hepatic *RAB24* levels are tightly associated with glucose and lipid homeostasis in humans.

Excess lipid accumulation leads to NAFLD with a possible progression to non-alcoholic steatohepatitis (NASH). To investigate the importance of Rab24 in more severe liver conditions, we checked the abundance of *RAB24* levels in independent liver samples of patients with NAFLD (-/+ steatosis), and NASH compared to healthy controls<sup>16</sup>. Interestingly, we found *RAB24* to be upregulated 64% and 75% in patients with NAFLD plus steatosis and NASH patients, respectively (**Fig. 1b**). The alterations in *RAB24* were

negatively correlated with whole body insulin sensitivity and positively correlated with hepatocellular lipids (**Extended Data Fig. 1c, d**). In addition, we observed a positive correlation with liver 8-oxo-guanosine ( $r=0.16$ ,  $p=0.036$ ) and IL6 ( $r=0.39$ ,  $p=0.039$ ) levels in these patients, markers that correspond to increase oxidative DNA damage and activation of cytokine pathways, respectively. Altogether, these data highlighted a relationship between higher Rab24 levels and an impaired metabolic state (lower whole body insulin sensitivity, high fat accumulation and inflammation) in humans.

### **Rab24KD improves glucose tolerance and serum lipid parameters**

To functionally explore Rab24, we administered lipid nano particles (LNPs) containing siRNA (against Rab24 or luciferase as control at 0.5 mg/kg each) via tail vein injection to silence Rab24 in liver<sup>14,15,17</sup>. Five days after injection, treatment with LNPs resulted in a 60% reduction in *Rab24* mRNA specifically in the liver (**Supplementary Fig. 1a**) and 75% reduction in Rab24 protein levels compared to control (**Supplementary Fig. 1b,c**). Rab24KD mice had similar body weight (**Supplementary Fig. 1d**), but showed a decrease in the liver to body weight ratio (**Supplementary Fig. 1e**). In agreement with the OGTT data from whole body KO mice, we observed an improvement of glucose clearance and a 15% reduction in the area under the curve (AUC) (**Fig. 1c, d**) of Rab24KD mice without affecting serum insulin levels and HOMA-IR (**Supplementary Fig. 1f, g**), highlighting the contribution of hepatic Rab24 to systemic glucose homeostasis. Insulin responsiveness was unchanged, as Rab24KD mice exhibited similar insulin tolerance compared to control (**Supplementary Fig. 1h**). Surprisingly, insulin-induced AKT activation in skeletal muscle, but not in liver or fat, was enhanced in Rab24KD animals, pointing towards a Rab24-dependent inter-organ communication pathway (**Fig. 1e, f** and **Supplementary Fig. 1i-k**). Indeed, expression and secretion of FGF21 was elevated in

primary mouse hepatocytes and mouse liver upon Rab24KD (**Fig. 1g-j**). Importantly, reduction of Rab24 in FGF21 homozygous KO mice caused no improvement in glucose clearance and insulin signaling in skeletal muscle compared to their heterozygous littermates, demonstrating an FGF21 dependent mechanism (**Fig. 1k-p**). Interestingly, liver but not fat of heterozygous FGF21 KO mice showed enhanced insulin-induced AKT activation upon Rab24 KD, which was abolished in the homozygous controls, suggesting an FGF21 dependent autocrine regulation (**Supplementary Fig. 1l-s**). We did not observe any alterations in brown adipose tissue (BAT) activation upon Rab24KD, indicating a BAT independent mechanism (**Supplementary Fig. 2a-h**).

Interestingly, KD of Rab24 also led to a decrease in serum total- and LDL cholesterol as well as ApoB (**Table 1**), suggesting an alteration of LDL uptake or secretion by the liver. Thus, LDL internalization kinetics were measured in primary hepatocytes with 60% reduction in mRNA and protein levels of Rab24 (**Supplementary Fig. 3a-c**) using a continuous uptake assay of fluorescently labeled DiI-LDL for various time points<sup>14,18</sup>. Rab24 KD caused a small increase in LDL endocytosis, which contributed to the improved serum LDL parameters (**Fig. 1q, r**), without affecting the expression of cholesterol transporters (**Supplementary Fig. 3d**), suggesting an increase in LDL trafficking. In addition to uptake, the liver is a major source of circulating cholesterol<sup>19</sup>. Interestingly, Rab24KD resulted in reduced cholesterol secretion from primary hepatocytes (**Fig. 1s**), and an increase in liver bile acid levels after 6 h starvation in Rab24KD mice (**Fig. 1t**). Altogether, these data provided *in vivo* evidence for an as-yet unknown role for hepatic Rab24 in the regulation of glucose and lipid handling.

### **Up-regulation of mitochondrial proteins upon Rab24 reduction**

To study mechanisms of Rab24 metabolic control, we performed quantitative proteomics analysis of liver tissues from control and Rab24KD mice. The tissues were subjected to liquid chromatography tandem mass spectrometry (LC MS/MS) and a combined analysis of the spectra from all samples resulted in the quantification of almost 5,000 proteins at a false discovery rate (FDR) of 1% using the label-free quantification algorithm in MaxQuant (**Table S1**). In a stringently filtered dataset for valid values of 3,600 proteins, we detected 622 differentially expressed proteins (DEP), of which 287 were up- and 335 downregulated compared to control-t-test ( $p$ -value<0.05) (**Table S1** and **Fig. 2a**). Next, we subjected the DEP to pathway enrichment analysis using KEGG and GO annotation (**Fig. 2b, c**). Most of the upregulated proteins were involved in metabolic processes, especially carbon and pyruvate metabolism, amino acid degradation and TCA cycle. Interestingly, most of those metabolic reactions are resident in the mitochondria. In agreement, we observed a strong up-regulation of mitochondria based on GO annotation. Interestingly, 101 mitochondrial proteins and 21 proteins involved in carbon metabolism were increased in abundance amongst the individual Rab24KD liver samples (**Table S2**). Proteins of the ribosomal pathway were downregulated. The remarkable increase in mitochondrial components prompted us to visualize the mitochondria distribution in the liver. Paraffin sections of Rab24KD livers revealed an app. 20% increase in the staining of the mitochondrial inner membrane marker prohibitin (**Fig. 2d, e**), suggesting an increase in mitochondrial mass. Altogether, these data indicated an upregulation of carbon metabolism and a pronounced increase in mitochondrial proteins upon Rab24KD.

### **Loss of Rab24 causes an increase in mitochondrial activity**

The striking effect on mitochondrial proteins inspired us to investigate the role of Rab24 on mitochondria function in primary hepatocytes *in vitro* and liver *in vivo*.

Interestingly, we observed an enhancement in the staining of the mitochondrial import factor Tom20 by quantitative immunofluorescence analysis (IF) *in vitro* and *in vivo*, supporting an increase in mitochondrial mass (**Fig. 3a-d**). This was confirmed by an up to 70% increase in mitotracker Green staining in primary hepatocytes and in isolated hepatocytes from control and Rab24 KD animals (**Fig. 3e, f**). To investigate whether the increase in mitochondria mass was associated with an improvement in mitochondrial function, we performed Seahorse analysis to measure the oxygen consumption rate (OCR) in primary mouse hepatocytes after Rab24KD. Interestingly, reduction of Rab24 *in vitro* led to an increase in the OCR, including basal respiration, ATP production and maximal respiration (**Fig. 3g, h**), revealing a regulatory role on mitochondrial function. Intriguingly, isolated primary hepatocytes from mice after *in vivo* KD of Rab24 displayed a similar induction in mitochondrial respiration, indicating an enhanced mitochondrial activity even in the liver (**Fig. 3i, j**). Supporting this observation, we also observed an increase in mitotracker Red staining in primary hepatocytes and in isolated hepatocytes from control and Rab24 KD animals (**Fig. 3k, l**). The induction in OCR was accompanied by a 25% increase in cellular ATP and enhanced reactive oxygen species (ROS) production (**Fig. 3m, n**). Despite the observed ROS elevation, we did not detect an increase in carbonylated proteins (**Fig. 3o**), indicating that the induced ROS levels upon Rab24KD were not damaging for the hepatocytes. Altogether, our data showed an induction of mitochondrial mass and respiration upon Rab24 depletion, highlighting a regulatory role of Rab24 in energy metabolism.

### **Reduction of Rab24 leads to enhanced glycolysis**

To test whether the increase in mitochondrial respiration was also affecting glycolytic flux, we investigated the effect of Rab24KD on glycolysis by measuring the

extracellular acidification rate (ECAR). Interestingly, we observed an increase in ECAR, basal glycolysis and glycolytic capacity in the Rab24KD hepatocytes, suggesting enhanced glycolytic activity (**Extended Data Fig. 2a, b**). The activation of glycolysis was strongly reduced by treatment with Antimycin A and Rotenone (AA/Rot), indicating the contribution of mitochondrial respiration. However, there was still a significant 30% difference in ECAR between control and Rab24KD cells after AA/Rot treatment, which was completely abolished by injection of 2-DG, suggesting an induction of glycolysis upon Rab24 KD. This is in agreement with our proteomics data, where we detected an up-regulation of glucokinase, phosphoglucomutase, pyruvate kinase and pyruvate dehydrogenase complex, indicating enhanced glycolysis (**Extended Data Fig. 2c**). The increase in glycolysis was accompanied with enhanced glucose uptake during the ECAR assay and upon extracellular glucose stimulations (**Extended Data Fig. 2d**). This can be explained by an elevation in *GLUT2* expression, but not *GLUT1 in vitro* and an increase in *GLUT1 in vivo* upon Rab24KD, suggesting differential activation of the glucose transporters (**Extended Data Fig. 2e, f**). Increase in ECAR caused a 20% accumulation of lactate in the medium upon Rab24KD, which further confirms an activation of glycolysis (**Extended Data Fig. 2g**). Interestingly, the effect of Rab24 was predominantly acting on anabolic glycolysis, as no effect on glucose production via gluconeogenesis was observed after Rab24KD *in vivo* (**Extended Data Fig. 2h**). Altogether, these data demonstrate that Rab24 reduction causes a mild increase in glycolysis and a strong activation of mitochondrial respiration.

### **Rab24KD increases mitochondrial connectivity by reducing fission**

To investigate how Rab24 regulates mitochondrial mass and activity, we first checked whether Rab24 affects mitochondrial biogenesis. Thus, we measured mRNA levels

of *PGC1 $\alpha$* , *PGC1 $\beta$* , *Nrf1* and *PPAR $\gamma$*  in primary hepatocytes *in vitro* and liver *in vivo* (**Supplementary Fig. 4a, b**) and observed no alterations upon Rab24KD, indicating that Rab24KD does not activate mitochondrial biogenesis.

Mitochondria are very dynamic organelles that undergo morphological adaptations to different nutritional conditions to optimize their ATP production depending on the external nutrient cues<sup>20</sup>. Thus, enhanced respiration and bioenergetics are associated with an increased mitochondrial network and elongation, which is induced under prolonged starvation<sup>21</sup>. On the other hand, nutrient overload induces a fragmentation of the mitochondrial network and a shift towards nutrient storage<sup>22</sup>. To test whether Rab24KD changed mitochondrial morphology, we employed electron microscopy (EM) analysis in liver tissues and primary hepatocytes to determine the density, surface area, perimeter (contour), form factor (complexity and branching of the mitochondria) and circularity (roundness) of the mitochondria<sup>23</sup>. Surprisingly, we observed a 10-30% increase in the mitochondria density, surface area, perimeter and form factor and  $\approx$ 10% decrease in the circularity upon Rab24KD *in vivo* (**Fig. 4a-f**) and *in vitro* (**Extended Data Fig. 3a-i**), indicating slightly bigger and more connected mitochondria. Importantly, the mitochondrial morphology appeared normal with similar levels of cristae structures, demonstrating an increase in healthy mitochondria (**Extended Data Fig. 3c, d**).

To further confirm an induction in mitochondria connectivity, we performed mitochondrial network analysis from deconvoluted images stained for Tom20 using the skeletonization analysis tool from Fiji. With this, fluorescence signal of deconvoluted images are detected and skeletonized, allowing quantitative measurements of Tom20 labeled mitochondrial outer membrane structures, including individual branches, junctions and length of branches of mitochondria. Remarkable, Rab24KD induced more connected mitochondria as evident in the zoomed deconvoluted images *in vivo* (**Fig. 4g, h**) and *in*

*vitro* (**Extended Data Fig. 4a**), characterized by a 50-70% increase in the number of branches and junctions per area as well as the length of branches (**Fig. 4i-k** and **Extended Data Fig. 4b-d**).

The accumulation of mitochondria density with a wider surface and better connectivity, without changing biogenesis, suggested an alteration in the mitochondria fusion/fission cycle<sup>24</sup>. Our proteomics analysis excluded alterations in the fusion machinery<sup>20</sup>, since Mitofusin I (Mfn1) and Optic Atrophy 1 (Opa1) protein levels were unchanged (**Extended Data Fig. 5a**). However, we observed significant reductions in the Mitofission regulatory protein 1 (Mtfr1) and the solute carrier family 25 member 46 (**Extended Data Fig. 5a**), which both are regulators of mitochondria fission<sup>25-27</sup>.

Fission is enhanced by ER/mitochondria interactions on organelle contact sites<sup>28,29</sup>. Thus, we stained primary mouse hepatocytes with the endoplasmic reticulum (ER) marker (KDEL) and the mitochondria marker (Tom20) and observed an enhanced co-localization upon Rab24KD (**Extended Data Fig. 5b** (left and middle panels)), measured by a 50% increase in the Pearson correlation between KDEL and Tom20 intensities (**Extended Data Fig. 5b** (right panels) and **c**), suggesting more contact between the ER and mitochondria when Rab24 was reduced. Mitochondria fission is induced by forming the fission complex, composed of Mitochondrial FISSion 1 protein (FIS1), Mitochondrial Fission Factor (Mff) and Mitochondrial Dynamics protein 49/51 (MiD49/51), which induces the activation and recruitment of dynamin-related protein 1 (DRP1) to the mitochondrial membrane<sup>30,31</sup>. Therefore, we stained primary hepatocytes for DRP1 and FIS1 and observed a 25% reduction in the mean fluorescence intensity/cell of DRP1 without affecting FIS1 (**Fig. 5a-c**), indicating inefficient recruitment of DRP1 upon loss of Rab24. Importantly, no change in protein levels of DRP1 was observed by proteomics, supporting a defect in subcellular localization (**Fig. 5d**). Indeed, we observed an equal decrease in the co-localization of

DRP1 with Tom20 measured by the Pearson correlation (**Fig. 5e, f**), indicating reduced DRP1 recruitment to the mitochondria upon Rab24KD. In agreement with the proteomics data, Mitofusin 1 and 2 were unaffected, supporting a preferential function of Rab24 on the fission machinery (**Extended Data Fig. 5d-f**). In fact, Rab24 has been shown to interact with FIS1 in mammalian cells (<https://thebiogrid.org/119817/summary/homo-sapiens/rab24.html>). To directly test this observation in liver, we performed pull-down experiments of GST-tagged Rab24 compared to a control Rab, Rab3a, using 12 h fasted and 12 h fasted plus 2 h refed liver lysates. Strikingly, we found a specific interaction of Rab24 with FIS1 but not with DRP1 in whole liver samples (**Fig. 5g**), supporting the biogrid interaction data. Importantly, no interaction with Rab3a was observed (**Fig. 5g**). These data indicate that Rab24 participates in regulating mitochondrial fission by directly interacting with FIS1.

If the connection of Rab24 to FIS1 was crucial for mitochondrial morphology and activity, interfering with FIS1 should mimic the Rab24KD phenotype on mitochondria. Rab24 only induced an app. 25% reduction in the assembly of the fission machinery; therefore we performed a KD of FIS1 with similar efficiency (**Extended Data Fig. 6a**). Reduction of FIS1 by 30% caused a rise in the basal respiration, ATP production and maximal respiration in primary hepatocytes (**Extended Data Fig. 6b-e**), induced by an increase in Tom20 intensity and mitochondrial connectivity (**Extended Data Fig. 6f-j**), supporting reduced fission and enhanced activity under mild FIS1KD conditions. Overall, these data underlined the conclusion that under physiological conditions Rab24 induces mitochondrial fission by directly interacting with FIS1, and that the inhibition of hepatic Rab24 reprograms mitochondrial turnover to boost mitochondrial connectivity and metabolic functions, ultimately leading to improvements in systemic metabolic health.

## **Rab24KD causes a reduction in mitophagy and increases autophagic flux**

Besides the function of mitochondrial fission in organelle plasticity under nutrient rich conditions, fission is required for mitochondrial degradation, in which damaged parts of the mitochondria are fissioned off and degraded via mitophagy<sup>31,32</sup>. Since Rab24 is affecting mitochondrial fission, we hypothesized that its reduction also alters mitophagy. To investigate this, we measured mitophagic flux under stress-induced conditions using the nucleoid depletion assay<sup>33,34</sup>. FCCP and oligomycin treatments induced a 34% reduction in cytoplasmic mtDNA particles in control cells, indicative of induced mitophagy (**Fig. 6a, b**). Interestingly, DNA depletion was reduced by 2-fold in Rab24KD cells upon FCCP and oligomycin treatment suggesting less mitochondrial degradation (**Fig. 6a, b**), which is in agreement with reduced mitochondrial fission. The reduction in mitophagy was confirmed by another assay that measures the accumulation of mitophagic vesicles upon FCCP treatment with and without chloroquine, where we observed a 20% reduction upon Rab24KD (**Extended Data Fig. 7a**). This was in agreement with electron microscopy data, where we detected already in the basal state less mitochondria engulfed by double membranes designated to fusion with lysosomes (**Fig. 6c, d**). Indeed, the colocalization of mitochondria labeled by Tom20 and lysosomes visualized by Lamp1 was significantly reduced measured by Pearson correlation analysis (**Extended Data Fig. 7b, c**), supporting less mitophagy upon Rab24KD, most likely due to a decrease in mitochondrial fission.

Rab24 has been shown to be involved in the autophagic pathway<sup>35</sup> and to be required for autophagosome clearance by interacting with lysosomes under nutrient rich conditions in cultured cancer cells<sup>12</sup>. To investigate whether Rab24KD also alters autophagic flux in primary hepatocytes *in vitro* and liver *in vivo*, we compared the levels of LC3-II and the autophagy receptor p62/SQSTM1 in fed, starved and starved plus chloroquine conditions (to prevent lysosomal degradation) by Western blotting and IF.

Starvation is a strong inducer of macroautophagy in the liver<sup>36</sup>, as evidenced by the increase in LC3-II between fasting and feeding in control cells and liver tissue (**Fig. 6e** and **Extended Data Fig. 8a, b**). Chloroquine (CQ) treatment induced additional accumulation of LC3-II, indicating increased degradation upon starvation *in vitro* and *in vivo* (**Fig. 6e** and **Extended Data Fig. 8a, b**). Upon Rab24 reduction, we observed no change in the fed state for LC3-II by IF and Western blot *in vitro* and by Western blot *in vivo* (**Fig. 6e** and **Extended Data Fig. 8a-c**) but a further increase of LC3-II upon chloroquine stimulation (**Fig. 6e** and **Extended Data Fig. 8a, b**), suggesting enhanced autophagy. Changes in autophagic flux can be measured by calculating the ratio of LC3-II levels in fasting plus chloroquine and fasting only conditions (fasted&CQ/fast) or by subtracting LC3-II levels in fasting from the fasting plus chloroquine conditions (fasted&CQ-fast) resulting in net LC3-II flux between samples (control vs. Rab24 KD)<sup>37</sup>. Using this assay, we measured a strong increase in LC3-II levels upon KD of Rab24 *in vitro* by Western blot and IF (**Fig. 6f, h-j**) and *in vivo* (**Fig. 6g**), demonstrating enhanced LC3-flux and net flux in the absence of Rab24.

The levels of p62 showed only a small increase in fasted control cells and tissues upon chloroquine treatment, suggesting minimal degradation of p62 under fasting conditions (**Extended Data Fig. 8d-h**). This is in agreement with p62's function in selective autophagy<sup>38</sup>, which is not activated upon fasting<sup>36</sup>. Therefore, p62 flux during starvation is low and does not contribute to the induction of bulk macroautophagy. The reduction of p62 in Rab24KD conditions (**Extended Data Fig. 8d-h**) is surprising and could have potential other reasons, such as transcriptional regulation<sup>39</sup>, however it has no consequence on the activation of autophagy under starvation in Rab24KD condition. The induction of autophagic flux was accompanied by an increase of LAMP1 positive structures by IF (**Extended Data Fig. 8i, j**), as indicated before<sup>40</sup>. Our result in primary mouse

hepatocytes and liver *in vivo* are in discrepancy with the previously observed reduction of autophagy upon Rab24KD<sup>40</sup>. However, this was only evident under full medium; upon amino acid starvation, a condition that physiologically activates autophagy, no effect of Rab24KD was observed<sup>40</sup>. This discrepancy indicates that Rab24 might fulfill different functions in autophagy in primary hepatocytes and mouse liver compared to stable-expressing Rab24 cell lines. Altogether our data demonstrate that Rab24KD increased p62-independent non-selective macroautophagy while decreasing mitochondrial fission and mitophagy, thereby boosting respiration, thus contributing to enhanced nutrient consumption.

### **Reduction of Rab24 improves glucose and lipid parameters in HFD mice**

To test whether the cellular functions of Rab24 translate into improvements of systemic metabolic health also in metabolically impaired conditions, we used a model of diet-induced obesity (DIO), feeding mice a HFD and elucidated the therapeutic possibility of reducing Rab24 levels for glucose and lipid metabolism. The HFD treated animals gained more weight and showed an increase in their fed blood glucose levels compared to low fat diet (LFD) treated animals (**Extended Data Fig. 9a, b**), consistent with the occurrence of obesity and hyperglycemia in this disease mouse model. Interestingly, we observed an induction of *Rab24* mRNA levels upon HFD (**Extended Data Fig. 9c**) in agreement with the human data (**Fig. 1a, b**). To examine the therapeutic potential of Rab24, we performed liver specific KD in 13 weeks HFD mice and measured a 80% reduction in Rab24 protein levels after 2 weeks of RNAi without affecting body weight (**Extended Data Fig. 9d, e**). Interestingly, reduction of Rab24 led to a decrease in serum cholesterol, LDL, ApoB (**Fig. 7a-c**) and triglyceride ( $p=0.06$ ) (**Extended Data Fig. 9f**) levels. Note that Rab24KD for 2 weeks did not completely reverse the hypercholesterolemia in HFD

mice compared to control, but contributed very significantly to an improvement in serum lipid parameters. In fact, serum ALT levels were completely restored (**Fig. 7d**) and liver lipid content strongly reduced (**Fig. 7e-g** and **Extended Data Fig. 9g-j**), highlighting the beneficial effect of Rab24 KD on overall liver health under a HFD. Interestingly, loss of Rab24 led to a decrease in the liver/body weight ratio (**Fig. 7h**), similar as observed in wild type mice (**Supplementary Fig. 1e**). The improvement in liver and serum lipids associated partly with lower fasting blood glucose levels in the HFD mice ( $p=0.07$ ) (**Fig. 7i**) and was accompanied by amelioration in their GTT and AUC after 4 weeks of LNP treatment (**Fig. 7j, k**). Importantly, Rab24 reduction in control LFD mice showed similar beneficial effects on serum lipid parameters without changing blood glucose levels, further strengthening the positive effects of diminishing Rab24 activity (**Extended Data Fig. 10a-h**).

To test whether the improved liver parameters were indeed associated with an induction in mitochondrial mass and connectivity, we performed IF in HFD treated liver sections and observed a strong increase in Tom20 staining upon Rab24KD (**Fig. 7l, m**), associated with more connected mitochondria (**Extended Data Fig. 4e-h**). In agreement, primary hepatocytes treated with the fatty acids (FA) oleate and palmitate for 3 days exhibited an increase lipid droplet formation evidenced by perilipin 2 (Plin2) staining compared to BSA alone, which was decreased upon Rab24 reduction (**Extended Data Fig. 9k**). Interestingly, Rab24KD hepatocytes treated with FA exhibited an increase in OCR, basal respiration and ATP production (**Extended Data Fig. 9i** and **Fig. 7n**), underscoring the beneficial effect of loss of Rab24 for liver lipid homeostasis and mitochondria respiration. Altogether, our data emphasized a potential therapeutic role of Rab24 in liver steatosis, glucose homeostasis and serum cholesterol levels in a model of diet induced obesity.

## Loss of Rab24 ameliorates liver steatosis and inflammation in NASH

As Rab24 was also upregulated in NASH patients, we performed knockdown experiments of Rab24 in mice under a methionine-reduced, choline-deficient (MCD) diet coupled to a high fat diet (MCD-HFD)<sup>41</sup>. The MCD-HFD model develops rapid steatosis and inflammation and progressive fibrosis<sup>41</sup>, but extenuate the severe weight loss of the usual MCD diet<sup>42</sup>. Interestingly, we observed a 30% upregulation of *Rab24* expression in MCD-HFD versus control LFD (**Fig. 8a**), supporting the human data (**Fig. 1b**). LNP based Rab24KD induced a 60% reduction in mRNA levels in the MCD-HFD group, supporting efficient KD of Rab24 in this mouse model (**Fig. 8a**). Interestingly, Rab24 KD improved the reduction in body weight and blood glucose in the MCD-HFD mice, suggesting a more healthy metabolic state of the animals (**Fig. 8b, c**). This was accompanied by a reduction in the liver to body weight ratio, which is usually induced due to the strong increase in steatosis in MCD-HFD mice (**Fig. 8d**). Indeed, reduction of Rab24 decreased liver steatosis and triglyceride content and improved serum ALT levels, indicating an improvement in liver health (**Fig. 8e-h**). Intriguingly, markers of NASH induction, such as *Acta2* (encoding alpha-smooth muscle actin, a marker of activated hepatic stellate cells) and *Adgre1* (encoding F4/80, a marker of murine macrophages) were also significantly reduced upon Rab24 KD (**Fig. 8i, j**). These data demonstrated a beneficial effect of reducing Rab24 in an early stage of NASH development.

## DISCUSSION

The importance of improving mitochondrial activity has been proven to be beneficial under conditions of diet-induced obesity and in diabetic animal models<sup>43,44</sup>, placing mitochondria at central stage of metabolic control. Mitochondrial activity is strongly regulated by mitochondria plasticity and turnover, which is controlled by nutrient

availabilities. Fasting inhibits mitochondria fission and consequently degradation by mitophagy and induces hyperfused mitochondria to ensure proper usage of energy substrates provided by autophagic pathways, when no external nutrients are available<sup>21</sup>. On the other hand, under postprandial conditions mitochondria fragment, mitophagy is induced and consequently mitochondria respiration decreases<sup>45,46</sup>.

Here we present data that strongly support Rab24 as a regulator of mitochondria turnover by underlining its role in the assembly of the fission machinery. We show that Rab24 directly interacts with FIS1, thereby ensuring efficient recruitment of DRP1 to mitochondrial membranes to drive the fission process. Reduction of Rab24 causes reduced mitochondria fission resulting in less mitophagy, increased mitochondria density and a more branched network capable of higher respiration. At the same time, we observe an induction of autophagic flux under Rab24KD, indicating enhanced energy usage. The induction of macro-autophagy combined with an enhanced mitochondrial network formation and activity are characteristics of liver starvation<sup>20</sup>. Therefore, we propose that Rab24KD reassembles the fasting state, in which mitochondria are metabolically reprogrammed towards higher respiration through enhanced connectivity and bioenergetics efficiency. On the other hand, the accumulation of Rab24 in the obese and NAFLD patients and obese mouse models could lead to a situation where autophagy is blocked<sup>47,48</sup> and mitochondria connectivity is reduced<sup>49,50</sup>, collectively contributing to enhanced energy storage. In fact, it has been shown that reduction in DRP1-mediated fission improves mitochondrial fitness in diabetes-related complications<sup>51,52</sup> and in Alzheimer's disease<sup>53</sup>. Clearly, completely reducing fission thus preventing mitophagy is not favorable for maintaining healthy mitochondria and cell survival. However, a slight reduction in fission, as shown for Rab24KD, can shift mitochondria to a more connected and active state and improve their function in diseases with reported mitochondrial dysfunctions.

Based on these data and our previous findings of a regulatory role of Rab5 on gluconeogenesis<sup>14,15</sup>, we propose another level of metabolic control through membrane trafficking regulators, which represents an emerging concept extending beyond liver metabolism<sup>6</sup>. In fact, the translocation of the glucose transporter 4 (GLUT4) in fat and muscle is dependent upon proper Rab10 function, which is fundamental for regulating glucose uptake in peripheral tissues<sup>54,55</sup>. In addition, variants in the clathrin heavy chain CHC22 in humans are associated with altered GLUT4 trafficking and correlate with features of type 2 diabetes<sup>56</sup>. Defective LDL uptake in the liver, due to altered LDLR trafficking in patients with mutations in the CCC complex (CCDC22) highlight the important contribution of trafficking regulators in hypercholesterolemia<sup>57</sup> and atherosclerosis in humans<sup>58</sup>. Altogether, these data emphasize a thus far rather unexplored connection between membrane transport processes and whole body energy homeostasis that has to be conceptually exploited for treatment options in type 2 diabetes and its related complications<sup>6</sup>.

## **METHODS**

### **Human samples**

In the first cohort, we investigated *RAB24* mRNA expression in liver tissue samples obtained from 40 extensively characterized Caucasian men (n=23) and women (n=17) with a wide range of body mass index (BMI: 22.7-45.6 kg/m<sup>2</sup>) who underwent open abdominal surgery for Roux en Y bypass, sleeve gastrectomy, elective cholecystectomy or explorative laparotomy. BMI was calculated as weight divided by squared height. Hip circumference was measured over the buttocks; waist circumference was measured at the midpoint between the lower ribs and iliac crest. Percentage body fat was measured by dual X-ray absorptiometry or bioimpedance analyses. In addition, abdominal visceral and SC fat areas were calculated using CT or MRI scans at the level of L4–L5. With oral glucose tolerance tests, we identified individuals with normal glucose tolerance (n=40). Methods of the phenotypic characterization have been described previously<sup>59</sup>. Insulin sensitivity was assessed with the euglycemic-hyperinsulinemic clamp method. After an overnight fast and resting for 30min in a supine position, intravenous catheters were inserted into antecubital veins in both arms of the participants. One line was used for the infusion of insulin and glucose, the other was used for frequent sampling of arterialized (heating pads) blood. After a priming dose of 1.2nmol/m<sup>2</sup> insulin, infusion with insulin (Actrapid 100U/ml, Novo Nordisk Bagsvaerd, Denmark) was started with a constant infusion rate of 0.28nmol/m<sup>2</sup> body surface per minute and continued for at least 120min. After 3min, the variable 20% glucose infusion rate was added and adjusted during the clamp to maintain a blood glucose level of 5.5 (± 5%) mmol/l. Bedside blood glucose measurements were carried out every 5min. Glucose infusion rate (GIR) was calculated from the last 45 min of the clamp, in which GIR could be kept constant to achieve the target plasma glucose concentration of 5.5 mmol/l. Therefore, the duration of the clamp varied between individuals (range 120–200

min). In premenopausal women, clamp studies were performed during the luteal phase of the menstrual cycle<sup>60</sup>.

All baseline blood samples were collected between 8 and 10 am after an overnight fast. Samples were immediately centrifuged and stored at -80°C until further analyses were performed. Plasma glucose levels were measured using the hexokinase method. Insulin was measured using chemiluminescence assay. High density lipoprotein (HDL) cholesterol and low density lipoprotein (LDL) cholesterol were measured using enzymatic assays (COBAS, Roche, Mannheim, Germany). CRP was quantified using an Image Automatic Immunoassay System (Beckman Coulter). Circulating levels of high-sensitivity interleukin 6 (hsIL 6), leptin (R&D Systems, Minneapolis, MN), and total adiponectin (ALPCO, Salem, NH) were determined in all blood samples with enzyme-linked immunosorbent assays (ELISAs) according to the manufacturers' instructions. The index for homeostatic model assessment of insulin resistance (HOMA1-IR) was calculated from fasting plasma insulin and glucose measurements.

All study protocols have been approved by the Ethics committee of the University of Leipzig (363-10-13122010 and 017-12-230112). All participants gave written informed consent before taking part in the study.

The second cohort comprised thirty-six obese individuals (OBE) undergoing bariatric surgery and 8 lean healthy humans (CON) undergoing elective surgery such as cholecystectomy or herniotomy (registered clinical trial NCT01477957), part of which were previously reported<sup>16,61</sup>. OBE were further classified into obese with steatosis (NAFL+), without steatosis (NAFL-), and NASH based on liver histology as described in<sup>16,61</sup>. They gave written informed consent before inclusion in the study, which was approved by the Heinrich-Heine-University Düsseldorf Institutional Review Board. All participants maintained stable body weight for at least 2 weeks before surgery and were

studied using hyperinsulinemic euglycemic clamps for measurement of peripheral and hepatic insulin sensitivity and blood sampling for routine lab parameters<sup>16</sup>. Participants were asked to refrain from physical activity for 3 days prior to the clamp test. Volunteers with severe renal, heart or lung disease, acute or chronic inflammatory condition or any history or signs of liver disease other than NAFLD were excluded from participation. Liver samples for measurement of liver fat content from histology, hepatic mitochondrial function and oxidative stress were obtained during surgery as described before<sup>16</sup>.

## **Animals**

All animal studies were conducted in accordance with German animal welfare legislation. Male C57BL/6N mice obtained from Charles River laboratories were maintained in a climate-controlled environment with specific pathogen-free conditions with 12-h dark/light cycles in the animal facility of the Helmholtz Center, Munich, Germany. Protocols were approved by the Institutional Animal Welfare Officer (Tierschutzbeauftragter), and necessary licenses were obtained from the state ethics committee and government of Upper Bavaria (55.2-1-55-2532-49-2017 and 55.2-1-54-2532.0-40-15). Mice were fed ad libitum with regular rodent chow. Mice for HFD studies received a HFD or LFD control from Research diets for 15 or 17 weeks, starting at the age of 4 weeks. Diet composition: LFD: 16% Protein, 73% Carbohydrate, 11% Fat in kcal; HFD: 16% Protein, 25% Carbohydrate, 58% Fat in kcal. Mice for NASH studies received a l-amino acid diet with 0.1 % Methionine and no added choline or LFD control from Research diets for 4 weeks starting at the age of 6 weeks. Diet composition: LFD: 18% Protein, 71% Carbohydrate, 10% Fat; MCD 18% Protein, 21% Carbohydrate, 62% Fat in kcal. All experiments were carried out in male mice with littermates as controls.

## **Antibodies and Reagents**

Primary antibodies were purchased from the following companies: Rab24 (ab154824), Mfn 1 (ab104274), Tom20 (ab78547), Vinculin (ab129002) & VCP (ab11433) from Abcam (Cambridge, UK), Tom20 (sc-11415) from Santa Cruz (Dallas, TX), Lamp1 (553792) & Drp1 (611112) from BD Bioscience (San Jose, CA), KDEL (ADI-SPA-827) from Enzo (Farmingdale, NY), AKT (9272), pAKT (4060) & Mfn2 (D1E9) (11925) from Cell Signaling Technology (New England Biolabs GmbH Frankfurt/Main, Germany), LC3b (L8918) from Sigma (Taufkirchen, Germany) for IF and LC3b (2775) from Cell Signaling (Frankfurt am Main, Germany) for western blot, p62 (6P62-C) and anti-DNA mouse monoclonal (61014) from progen (Heidelberg, Germany) and Fis1 (HPA017430) from Atlas Antibodies (Bromma, Sweden). Bodipy 493/503, Mito Tracker green FM and red CM-H<sub>2</sub>Xros, secondary antibodies labeled with Alexa fluorophores and Alexa-488-phalloidin were obtained from Thermo Fisher Scientific (Waltham, MA). HRP tagged secondary antibodies against mouse or rabbit were purchased from Thermo Fisher Scientific (Waltham, MA) & Sigma-Aldrich (Taufkirchen, Germany) respectively. LDL was purified from human serum and labeled with DiI and DiD<sup>62</sup>.

## **Rab24 silencing via lipid nanoparticles (LNP)**

LNPs containing siRNA targeting Rab24 or Luciferase as control were manufactured by Axolabs (Kulmbach, Germany). Rab24: Sense 5'-gaAuAcGuGGGcAaGAcGAdTsdT-3', Antisense 5'-UCGUCUUGCCcACGuAUUCdTsdt-3'; Luciferase: Sense 5'-cuuAcGcuGAGuAcuucGAdTsdt-3', Antisense 5'-UCGAAGuACUcAGCGuAAGdTsdt-3'. A, G, U, C: RNA Nucleotide; dA, dG, dT, dC: DNA Nucleotides; a, g, u, c: 2'-O-Methyl-Nucleotide; s: Phosphorothioate

siRNAs with canonical structures were directed against the full-length Rab24 mRNA and perfectly matched to all known mRNA transcript variants (NM\_009000.3, XM\_006517165.3, ENSMUST00000035242) of the target gene available in the NCBI reference sequence database (release 79) and the Ensembl project database (release 85). The siRNAs used in this study were designed to be a perfect match only to their target mRNA and to have  $\geq 2$  mismatches within positions 2–18 of the 19-mer antisense strand sequence to any other genes. The siRNA antisense strands lacked a seed region (nucleotides 2–7) identical to a seed region (nucleotides 2–7) of known mouse miRNAs (miRBase, release 21). From siRNAs fulfilling those criteria, 12 siRNAs for final screening were selected for predicted activity based on analysis with proprietary algorithms (Axolabs, Kulmbach, Germany).

siRNAs were obtained from LGC Axolabs (Kulmbach, Germany). Briefly, RNA oligonucleotides were synthesized on solid phase made of controlled pore glass (CPG)(Prime Synthesis, Aston, PA) using commercially available 5'-O-(4,4'-dimethoxytrityl)-3'-O-(2-cyanoethyl-N,N-diisopropyl) phosphoramidite monomers of uridine (U), 4-N-acetylcytidine (CAc), 6-N-benzoyladenosine (Abz) and 2-N-isobutylguanosine (GiBu) with 2'-O-t-butyldimethylsilyl (SAFC Proligo, Hamburg, Germany) protection according to standard phosphoramidite oligomerization methodology. 2'-O-methyl-modifications were introduced employing the corresponding phosphoramidites carrying the same nucleobase protecting groups as the regular RNA building blocks. Syntheses were carried out on K&A DNA/RNA synthesizers (K&A Laborgeraete, Schaafheim, Germany). Coupling time for all phosphoramidites (0.1 M in Acetonitrile (SAFC Proligo, Hamburg, Germany)) was 4 min employing 5-Ethylthio-1H-tetrazole (ETT) (Biosolve, Dieuze, France) as activator (0.5 M in Acetonitrile). Phosphorothioate linkages were introduced using commercially available 3-

((Dimethylamino-methylidene)amino)-3H-1,2,4-dithiazole-3-thione (DDTT) (AM Chemicals, Oceanside, CA). Oligonucleotides were synthesized “DMT off” and deprotection was carried out according to published procedures<sup>63</sup>. Crude oligonucleotides were purified by anion-exchange high-performance liquid chromatography (HPLC) and analyzed by RP HPLC for purity and ESI mass spectrometry for identity. To generate siRNAs from RNA single strands, equimolar amounts of complementary sense and antisense strands were mixed and annealed in a 20 mM NaCl (Sigma-Aldrich Taufkirchen, Germany), 4 mM sodium phosphate pH 6.8 buffer (Sigma-Aldrich Taufkirchen, Germany). siRNAs were further characterized by size exclusion HPLC and were stored frozen until use.

1,2-distearoyl-3-phosphatidylcholine (DSPC) was purchased from Avanti Polar Lipids (Alabaster, Alabama, USA).  $\alpha$ -[3'-(1,2-dimyristoyl-3-propanoxy)-carboxamide-propyl]- $\omega$ -methoxy-polyoxyethylene (PEG-c-DOMG) was obtained from NOF (Bouwelven, Belgium). Cholesterol was purchased from Sigma-Aldrich (Taufkirchen, Germany). Stock solutions of XL521 lipid, DSPC, cholesterol, and PEG-c-DOMG were prepared at concentrations of 50 mM in ethanol (Sigma-Aldrich Taufkirchen, Germany) and stored at -20°C. The lipids were combined to yield molar ratio of 50:10:38.5:1.5 (XL: DSPC: Cholesterol: PEG-c-DOMG) and diluted with ethanol to a final lipid concentration of 25 mM. siRNA stock solutions at a concentration of 10 mg/mL in H<sub>2</sub>O were diluted in 50 mM sodium citrate (Sigma-Aldrich Taufkirchen, Germany) buffer, pH 3.

The nanoparticles formulations were prepared by combining the lipid solution with the siRNA solution at total lipid to siRNA weight ratio of 7:1. The lipid ethanolic solution was rapidly injected into aqueous siRNA solution to afford a suspension containing 33% ethanol. The solutions were injected by the aid of a syringe pump (Harvard Pump 33 Dual Syringe Pump Harvard Apparatus Holliston, MA). Subsequently, the formulations were

dialyzed 2 times against phosphate buffered saline (PBS), pH 7.4 at volumes 200-times of the primary product using a Slide-A-Lyzer cassettes (Thermo Fisher Scientific, Rockford, IL) with a MWCO of 10 kD (RC membrane) to remove ethanol and achieve buffer exchange. The first dialysis was carried at room temperature for 3 h and then the formulations were dialyzed overnight at 4°C. The resulting nanoparticle suspension was filtered through 0.2 µm sterile filter (Sarstedt, Nümbrecht, Germany) into glass vials and sealed with a crimp closure.

Particle size and zeta potential of formulations were determined using a Zetasizer Nano ZS (Malvern Instruments Ltd, Malvern, Worcestershire, UK) in 1X PBS and 15 mM PBS, respectively. The siRNA concentration in the liposomal formulation was measured by UV-vis. Briefly, 100 µL of the diluted formulation in 1X PBS was added to 900 µL of a 4:1 (v/v) mixture of methanol (Sigma-Aldrich Taufkirchen, Germany) and chloroform (Sigma-Aldrich Taufkirchen, Germany). After mixing, the absorbance spectrum of the solution was recorded between 230 nm and 330 nm on a DU 800 spectrophotometer (Beckman Coulter, Beckman Coulter, Inc., Brea, CA). The siRNA concentration in the liposomal formulation was calculated based on the extinction coefficient of the siRNA used in the formulation and on the difference between the absorbance at a wavelength of 260 nm and the baseline value at a wavelength of 330 nm.

Encapsulation of siRNA by the nanoparticles was evaluated by the Quant-iT™ RiboGreen® RNA assay (Invitrogen Corporation Carlsbad, CA). Briefly, the samples were diluted to a concentration of approximately 5 µg/mL in TE buffer (10 mM Tris-HCl, 1 mM EDTA, pH 7.5) (Sigma-Aldrich Taufkirchen, Germany). 50 µL of the diluted samples were transferred to a polystyrene 96 well plate, then either 50 µL of TE buffer or 50 µL of a 2% Triton X-100 (Sigma-Aldrich Taufkirchen, Germany) solution was added. The plate was incubated at a temperature of 37°C for 15 minutes. The RiboGreen reagent was diluted

1:100 in TE buffer, 100  $\mu$ L of this solution was added to each well. The fluorescence intensity was measured using a fluorescence plate reader (Wallac Victor 1420 Multilabel Counter; Perkin Elmer, Waltham, MA) at an excitation wavelength of  $\sim$ 480 nm and an emission wavelength of  $\sim$ 520 nm. The fluorescence values of the reagent blank were subtracted from that of each of the samples and the percentage of free siRNA was determined by dividing the fluorescence intensity of the intact sample (without addition of Triton X-100) by the fluorescence value of the disrupted sample (caused by the addition of Triton X-100).

Hepa1-6 cells were obtained from ATCC (in partnership with LGC Standards, Wesel, Germany) and cultured in ATCC-formulated Dulbecco's Modified Eagle's Medium (ATCC in partnership with LGC Standards, Wesel, Germany) supplemented to contain 10% fetal calf serum (Ultra-low IgG from Life technologies (Darmstadt, Germany) and 1% Pen/Strep (Biochrom GmbH, Berlin, Germany) at 37°C in an atmosphere with 5% CO<sub>2</sub> in a humidified incubator. For transfection of Hepa1-6 cells with siRNA, Hepa1-6 cells were seeded at a density of 20000 cells/well in 96-well regular tissue culture plates. Transfection of siRNA was carried out with Lipofectamine2000 (Life technologies, Darmstadt, Germany) according to manufacturer's instructions. Dose-response experiments were done with final Rab24 siRNA concentrations of 24, 6, 1.5, 0.375, 0.0938, 0.0234, 0.0059, 0.0015, 0.0004, and 0.0001 nM. Control wells were transfected with F-Luc, R-Luc or Aha-1 siRNA, or mock treated. For each siRNA and controls, four wells were transfected in parallel, and individual data points were collected from each well. 24 h post-transfection, media was removed and cells were lysed in 150  $\mu$ l Lysis Mixture (1 volume lysis mixture, 2 volumes nuclease-free water) and then incubated at 53 °C for 60 minutes. Branched DNA (bDNA) assay was performed according to manufacturer's instructions (Thermo Fisher Scientific, Waltham, MA). Luminescence was read using 1420 Luminescence Counter

(WALLAC VICTOR Light, Perkin Elmer, Rodgau-Jügesheim, Germany) following 30 min incubation in the dark. For each well, the Rab24 mRNA level was normalized to the GAPDH mRNA level. The activity of a given Rab24 siRNA was expressed as percent Rab24 mRNA concentration (normalized to GAPDH mRNA) in treated cells, relative to the mean Rab24 mRNA concentration (normalized to GAPDH mRNA) averaged across control wells.

### ***In vivo* LNP injections**

Eight weeks old male C57BL/6N mice, 36 weeks old male FGF21 KO mice (C57BL/6 background)<sup>64,65</sup> and heterozygous male littermates as control or male C57BL/6N mice fed a HFD for 13 weeks (HFD starting at the age of 4 weeks) received either PBS or siRNA in LNP formulations (either Rab24 or Luciferase control) at 0.5 mg/kg via tail vein injection as described before<sup>14,15,66,67</sup>. IpGTTs, ipPTTs and ipITTs were performed in C57BL/6N mice 5 days post injection using 2 g/kg glucose, 2 g/kg pyruvate or 0.75 U/kg insulin (Lilly, Indianapolis, IN) after starvation of 6 h for GTT and ITT or 16 h for PTT. On day 6 post injection, after 6 h fasting mice were sacrificed using cervical dislocation and serum and tissue was harvested and snap frozen in liquid nitrogen. HFD mice were treated for 2 (for lipid parameters) or 4 (for ipGTT) weeks with weekly injection of LNPs starting at 13 weeks of HFD. Male C57BL/6N Mice on MCD diet were injected weekly contemporaneously to the diet starting at 6 weeks of age.

For studying insulin sensitivity of liver and peripheral tissue, mice starved for 6 h were injected with 0.75 U/kg insulin or PBS and sacrificed after 7 min by freeze clamping. Liver, gastrocnemius muscle and epididymal fat were harvested for Western blot analysis.

For all studies LNPs at 0.5 mg/kg were injected through tail vein.

## **Serum Parameters**

Serum insulin levels were obtained with the Mouse Insulin ELISA kit (Alpco, Salem, NH) according to manufacturer's instructions. FGF21 levels in serum were measured with Mouse/Rat FGF21 Quantikine Kit from R&D Systems (Minneapolis, MN). For estimation of albumin, ALT, Apo A, Apo B, AST, total cholesterol, HDL, LDH, LDL, total protein and triglyceride serum levels, Luciferase control and Rab24 KD mice were sacrificed 5 days post LNP injection. Blood was collected and serum acquired by centrifugation (10 min, 10 000 x g). Parameters were measured using the Beckman Coulter (Brea, CA) Serum Analyzer AU480.

## **Proteomics & Bioinformatics**

For proteomics analysis, liver tissue from Luciferase control and Rab24 KD mice, starved for 6h, was obtained 5 days after LNP injection and snap frozen in liquid nitrogen. 50 µg protein were solubilized in 3x volume of lysis buffer (4% sodium deoxy cholate (SDC), 100 mM Tris pH 8.5, heated for 5 min at 95 °C, and sonicated (Branson probe sonifier output 3-4, 50% duty cycle, 3× 30s). Proteins were reduced and alkylated for 15 min at room temperature with 10 mM tris-(2-carboxyethyl)-phosphin-hydrochlorid (TCEP) and 40 mM 2-chloroacetamide (CAA) and digested with LysC and trypsin 1:50 (protein:enzyme) overnight at 37 °C. The digested peptides were acidified to a final concentration of 1% TFA. The peptide solution was cleared by centrifugation and loaded onto activated (30% Methanol, 1% TFA) double layer styrenedivinylbenzene–reversed phase sulfonated STAGE tips (SDB-RPS; 3M Empore)<sup>64</sup>. The STAGE tips were first washed with 200 µl 0.2% TFA, then with 200 µl 0.2% TFA and 5% ACN. The peptides were eluted with 60 µl SDB-RPS elution buffer (80% ACN, 5% NH<sub>4</sub>OH) for single shot analysis.

For MS analysis 2  $\mu\text{g}$  peptides were loaded onto a 50-cm column with a 75  $\mu\text{M}$  inner diameter, packed in-house with 1.9  $\mu\text{M}$  C18 ReproSil particles (Dr. Maisch GmbH) at 60  $^{\circ}\text{C}$ . The peptides were separated by reversed-phase chromatography using a binary buffer system consisting of 0.1% formic acid (buffer A) and 80% ACN in 0.1% formic acid (buffer B). Peptides were separated on a 120 min gradient (5-30% buffer B over 95 min, 30-60% buffer B over 5 min) at a flowrate of 300 nl on an EASY-nLC 1200 system (Thermo Fisher Scientific, Waltham, MA). MS data were acquired using a data dependent top-15 method with maximum injection time of 20 ms, a scan range of 300–1650 Th, and an AGC target of  $3\text{e}6$ . Sequencing was performed via higher energy collisional dissociation fragmentation with a target value of  $1\text{e}5$ , and a window of 1.4 Th. Survey scans were acquired at a resolution of 60,000. Resolution for HCD spectra was set to 15,000 with maximum ion injection time of 28ms and an underfill ratio of either 20% or 40%. Dynamic exclusion was set to 30s.

Raw mass spectrometry data were processed with MaxQuant version 1.5.6.4 using default setting if not stated otherwise. False-discovery rate (FDR) at the protein, peptide and modification level was set to 0.01. Oxidized methionine (M) and acetylation (protein N-term) were selected as variable modifications, and carbamidomethyl (C) as fixed modification. Three missed cleavages for protein analysis and five for phosphorylation analysis were allowed. Label free quantitation (LFQ) and “Match between runs” were enabled. Proteins and peptides were identified with a target-decoy approach in revert mode, using the Andromeda search engine integrated into the MaxQuant environment. Searches were performed against the mouse UniProt FASTA database (September 2014) containing 51,210 entries. Quantification of peptides and proteins was performed by MaxQuant. Bioinformatics analysis was performed with Perseus 1.5.4.2. Annotations were extracted

from UniProtKB, Gene Ontology (GO), and the Kyoto Encyclopedia of Genes and Genomes (KEGG).

For proteome analysis, quantified proteins were filtered for at least three valid values among four biological replicates in at least one of the conditions (Control and Rab24 KD). Missing values were imputed from a normal distribution with a downshift of 0.3 and a width of 1.8. Significantly up-or-downregulated proteins were determined by Student's t-test (FDR 0.05). Hierarchical clustering, 1D annotation enrichment, and Fisher's exact test were performed in Perseus.

### **Pulldown assay**

Rosetta<sup>TM</sup>(DE) Escherichia coli competent cells were transformed with pET-60-DEST<sup>TM</sup> (Novagen). Expression of GST-Rab24 and GST-Rab3a was induced by 1 mM IPTG at an optical density (600 nm) of 0.5 and bacteria was incubated for 4 h at 37°C. Bacteria pellets were resuspended in lysis buffer (20 mM HEPES pH 7.5, 100 mM NaCl, 2 mM MgCl<sub>2</sub>, 100 µg/mL lysozyme) followed by incubation for 30 min at 4°C. After adding 0.1 mM PMSF and 1 mM DTT, bacteria lysis was obtained by sonication at an amplitude of 50 % for 5 min (30 sec sonication and 30 sec break). Batch purification of GST-tagged proteins was performed on Glutathione Sepharose 4B (GE Healthcare). Beads were equilibrated with purification buffer (20 mM HEPES pH 7.5, 100 mM NaCl, 2 mM MgCl<sub>2</sub>) and bacteria lysates were incubated on beads (50:1) overnight at 4°C with end-over-end rotation. Loaded beads were then washed 5 x in purification buffer. Purity of GST-Rab24 and GST-Rab3a was analyzed by mass spectrometry.

Liver tissue from mice was prepared in RIPA buffer (50 mM Tris/HCl pH 8.0, 150 mM NaCl, 0.1 % SDS, 0.5 % sodium deoxycholate, 1% NP-40) supplemented with protease and phosphatase inhibitors (Roche cOmplete<sup>TM</sup>). Tissue was homogenized at 4 ms

speed for 20 sec (Omni Bead Ruptor 24), filtered through a 4.5  $\mu\text{m}$  PVDF membrane (Merck Ultrafree®-CL) and protein concentration was adjusted to 5  $\mu\text{g}/\mu\text{L}$ .

Nucleotide exchange was obtained by incubating mouse liver lysates with 1 mM EDTA for 10 min at 37°C followed by 10 min at 37°C in presence of 5 mM  $\text{MgCl}_2$  and 1 mM GMP-PNP or GDP- $\beta$ -S. Nucleotide exchange for immobilized GST-Rab24 and GST-Rab3a was performed as described before by Vitale et al<sup>65</sup>. Briefly, recombinant Rab proteins were incubated with nucleotide buffer (50 mM Tris/HCl pH 8.0, 150 mM NaCl, 5 mM  $\text{MgCl}_2$ , 1 mM EDTA, 1 mM GMP-PNP or GDP- $\beta$ -S) for 1 h at RT followed by an incubation with stabilization buffer (50 mM Tris/HCl pH 8.0, 150 mM NaCl, 2 mM  $\text{MgCl}_2$ , 1 mM GMP-PNP or GDP- $\beta$ -S) for 10 min at RT with rotation. For protein binding, prepared mouse liver lysates were supplemented with 1 % glycerol and then incubated on GST-Rab24 or GST-Rab3a beads for 1 h at RT under rotation with each batch having the corresponding nucleotide state. Beads were washed 3 x in wash buffer (50 mM Tris/HCl pH 8.0, 150 mM NaCl, 2 mM  $\text{MgCl}_2$ , 10  $\mu\text{M}$  GMP-PNP or GDP- $\beta$ -S, protease and phosphatase inhibitor). Proteins bound to GST-Rab24 or GST-Rab3a were detected by SDS-PAGE and subsequent immunoblotting using the antibodies Fis1 (HPA017430) from Atlas Antibodies and Drp1 (611112) from BD.

### **Triglyceride concentration**

To measure the amount of triglycerides stored in the liver of Luciferase and Rab24 KD mice, liver tissue was snap frozen in liquid nitrogen 5 days after LNP injection and the triglyceride amount quantified with the Triglyceride assay kit from abcam, according to manufacturer's instructions.

### **Human *RAB24* mRNA expression studies**

Human *RAB24* mRNA expression was measured by quantitative real-time RT-PCR in a fluorescent temperature cycler using the TaqMan assay, and fluorescence was detected on an ABI PRISM 7000 sequence detector (Applied Biosystems, Darmstadt, Germany). Total RNA was isolated using TRIzol (Life technologies, Grand Island, NY). Quantity and integrity of RNA was monitored with NanoVue plus Spectrophotometer (GE Healthcare, Freiburg, Germany). 1 µg total RNA from liver tissue samples was reverse-transcribed with standard reagents (Life technologies, Darmstadt, Germany). cDNA was then proceeded for TaqMan probe-based quantitative real-time polymerase chain reaction (qPCR) using the QuantStudio 6 Flex Real-Time PCR System (Life Technologies, Darmstadt, Germany). mRNA expression was measured by quantitative real-time RT-PCR using human the following probe for *RAB24* (Hs01585710\_g1). Fluorescence emissions were monitored after each cycle. Human *RAB24* mRNA expression was calculated relative to the mRNA expression of *18S rRNA* (Hs99999901\_s1).

#### **qPCR analysis using SYBRgreen**

Liver tissue or cultured primary hepatocytes were lysed using TRIzol (Life technologies, Darmstadt, Germany) to extract RNA. cDNA was transcribed using the SuperScript III reverse transcriptase kit from Life technologies (Darmstadt, Germany). RT-PCR was conducted in 10 µl of total reaction volume containing SYBRgreen (Life technologies, Darmstadt, Germany), 200 nM of forward and reverse primers (Table S3) and 24 ng of total cDNA. The reaction was performed using the Quantstudio6 (Life Technologies, Darmstadt, Germany) with the thermal cycling conditions: 50 °C for 2 min; 95 °C for 10 min; 95 °C for 15 s and 60 °C for 1 min (40 Cycles). Relative mRNA levels were quantified by calculating the comparative 2- $\Delta\Delta$  CT Method.

## **Western blot and Quantification**

For western blot analysis 20/ 40 µg of liver lysates or cultured primary hepatocytes, lysed with SDS-lysis buffer (20 mM Tris pH 7.5 (Roth, Karlsruhe, Germany), 150 mM NaCl (Roth, Karlsruhe, Germany), 1 mM EDTA (Roth, Karlsruhe, Germany), 1 mM EGTA (Sigma-Aldrich Chemie, Munich, Germany), 1% SDS, 1% Na-deoxycholate (Sigma-Aldrich Chemie, Munich, Germany)) supplemented with Phosstop (Sigma-Aldrich Chemie, Munich, Germany) were run in SDS/PAGE gels (Novex WedgeWell 8-16% Tris-Glycine Mini Gels) (Thermo Fisher Scientific, Waltham, MA), transferred to nitrocellulose membranes (Chicago, IL) and incubated with different antibodies (see antibodies and reagents). Protein bands were detected using Amersham ECL Prime (Th. Geyer, Renningen, Germany) with a BioRad Chemidoc MP imaging system and quantified with Image Lab (BioRad, Hercules, CA) and ImageJ using the method outlined at <http://lukemiller.org/index.php/2010/11/-analyzing-gels-and-western-blots-with-image-j>.

## **Histology**

Liver pieces of Luciferase control and Rab24 KD mice were harvested 5 days after LNP administration and snap frozen in liquid nitrogen. Excised specimens were fixed in 4% (w/v) neutrally buffered formalin (Sigma-Aldrich Chemie, Munich, Germany), embedded in paraffin (SAV, Flintsbach, Germany) and cut into 3 µm slices for H&E staining or for immunohistochemistry. Immunohistochemical staining was performed under standardized conditions on a Discovery XT automated stainer (Ventana Medical Systems, Tucson, AZ) using rabbit anti-prohibitin (1:200, Abcam28172; Abcam, Cambridge, UK) as a primary antibody and Discovery Universal (Ventana Medical Systems, Tucson, AZ) as secondary antibody. Signal detection was conducted using the Discovery® DAB Map Kit (Ventana Medical Systems, Tucson, AZ). The stained tissue sections were scanned with an

AxioScan.Z1 digital slide scanner (Zeiss, Jena, Germany) equipped with a 20x magnification objective. Images were evaluated using the commercially available image analysis software Definiens Developer XD 2 (Definiens AG, Munich, Germany) following a previously published procedure<sup>66</sup>. The calculated parameter was the mean brown staining intensity of the stained tissue.

For cryostat sections, control and Rab24KD livers were defrosted in 4% PFA, rotated in 4% PFA at 4 °C over night and placed in PBS until further use. Before embedding them in optimal cutting temperature compound OCT, liver pieces were transferred to 30% sucrose for 3 days. Then, 5 to 7 µm cryostat sections were cut and collected on superfrost plus treated slides. Cryosections were immunolabelled with first and secondary antibodies incubated in PBS BSA (3 %) for 2 h and 1 h respectively at room temperature. Then, sections were mounted with mowiol onto coverslip.

### **Hepatocyte isolation and transfection**

Primary hepatocytes were isolated via collagenase perfusion from 8-12 weeks old male C57BL/6N mice<sup>67</sup>. Briefly, mice were anaesthetized, both abdominal walls were opened and the liver was perfused through the *venae cavae* with EGTA-containing HEPES/KH buffer for 10 min, followed by a collagenase containing HEPES/KH buffer for 10 – 12 min until liver digestion is visible. The perfused liver is cut out and placed into a suspension buffer containing dish and hepatocytes are gently washed out. After filtering the cells through a 100 nm pore size mash, the cells are centrifuged and washed twice and re-suspended in suspension buffer. For a detailed isolation protocol including pictures please see Godoy et al.<sup>68</sup>

200 000 cells per well were plated in collagen coated 24-well plates (Thermo Fisher Scientific, Waltham, MA) in Williams E Medium (PAN Biotech, Aidenbach, Germany)

containing 10% FBS (PAN Biotech, Aidenbach, Germany), 5% penicillin/ streptomycin (Life Technologies, Darmstadt, Germany) and 100 nM dexamethasone (Sigma-Aldrich Chemie, Munich, Germany) and maintained at 37 °C and 5% CO<sub>2</sub>. After 1 hour cells were washed with phosphate buffer saline (PBS) (Life Technologies, Darmstadt, Germany) and incubated with 40 nM siRNA (Rab24 and ATG7) or 0.1 nM Fis1 (Rab24 obtained from Axolabs, Kulmbach, Germany, Fis1 and ATG7 from Dharmacon, Lafayette, CO), Interferin (1.2 µl/well) (Biomol, Hamburg, Germany) in Williams E medium. After 6 h of incubation cells were washed with PBS and a second layer of collagen was added to maintain cells in a sandwich culture. Williams E medium was changed twice a day<sup>15,18</sup>.

HFD *in vitro* conditions were obtained by supplementing Williams E medium with 100 µM Palmitate and 400 µM Oleate (both conjugated with BSA 1:6) (Sigma-Aldrich Chemie, Munich, Germany) or the respective amount of BSA.

### **Electron microscopy**

Electron microscopy (EM) was performed at the CCMA EM Core Facility (Université de Nice Sophia Antipolis, France). Primary hepatocytes silenced or not for Rab24, were fixed in 2.5% glutaraldehyde (GA) (Electron Microscopy Sciences, Hatfield, PA) overnight at room temperature. Then the cells were post-fixed in potassium ferrocyanide-reduced osmium tetroxide (Electron Microscopy Sciences, Hatfield, PA) for 1 h, and dehydrated in bath with increasing concentration of ethanol (VWR, Radnor, PA). The cells were incubated with mixture of epon:ethanol (1:2 and 2:1) and finally embedded with pure epon (Electron Microscopy Sciences, Hatfield, PA)<sup>14,17</sup>. Sections of 70nm were performed on a Leica ultramicrotome and counter-stained with uranyl acetate and lead citrate. Images of at least 30 cells per conditions were acquired.

Numbers of mitochondria were counted manually for each image and the areas were analyzed by using Fiji software. For the morphological description of the mitochondria, the area, perimeter, width, height and feret's diameter were extracted from Fiji by segmenting manually the mitochondria. Then these values were used to calculate the mitochondria form factor ( $\text{perimeter}^2/(4\pi\text{Area})$ ), the mitochondrial aspect ratio (width/ height), mitochondria circularity ( $4\pi(\text{area}/\text{perimeter})$ ) and mitochondria roundness ( $4(\text{area}/(\pi\text{width}))$ )<sup>69</sup>. Numbers of mitophagy event, easily recognizable by morphology, were counted manually on the same set of images, and reported to the area analyzed.

### **Immunofluorescence and LDL uptake assay**

For IF, cells in sandwich culture were fixed 3 days post plating in 4% PFA at RT for 30min, subsequently washed with PBS twice, permeabilized for one hour with 0.1% Triton X-100 (Applichem, Darmstadt, Germany), washed and blocked for 2 h in 10% horse serum (Thermo Fisher Scientific, Waltham, MA)<sup>18</sup>. Over night cells were incubated with secondary antibodies at 4°C, washed for 2 h with TrisHCL (pH 8.0, 10 mM) (Roth, Karlsruhe, Germany) and NaCl (300 mM) (Roth, Karlsruhe, Germany) -Tween-Solution (0.1%) (Sigma-Aldrich Chemie Munich, Germany) (TNT) and incubated with secondary antibodies (1:1000) and phalloidin (1:200) (Thermo Fisher Scientific, Waltham, MA) for 5 h at 37 °C. Cells were washed twice with PBS, incubated with DAPI (1:10000) (Thermo Fisher Scientific, Waltham, MA) for 5 min then mounted onto glass slides with 0.1 g/ml Mowiol (Merck, Darmstadt, Germany).

Cells in monolayer culture were fixed for 15 min in PFA, washed twice for 5 min in PBS and permeabilized in 0.1 % Triton X-100 in PBS for 10 min at RT. After two more washes for 5 min in PBS, cells were blocked in 10 % horse serum for 10 min at RT and subsequently treated with primary antibodies in 5 % horse serum for 1 h. Cells were

washed 3 times for 5 min in PBS and incubated 1 h with secondary antibodies (1:1000) at RT. Subsequently cells were washed twice with PBS and stained with Dapi, then mounted onto glass slides with 0.1 g/ml Mowiol.

For the LDL uptake assay, cells were starved for 2 h in Williams E w/o serum or dexamethasone. Continuous uptake of DiI-LDL (~2.5 µg/ml) for several time points was performed, cells were washed with cold PBS and fixed in 4% paraformaldehyde<sup>14</sup>. Cells were stained with DAPI and mounted with Mowiol.

### **Confocal microscopy and analysis**

Immunofluorescent samples were analyzed using a Laser Scanning Confocal Microscope (Olympus Fluoview 1200, Olympus, Tokyo, Japan) equipped with an Olympus UPlanSApo 60x 1.35 and an UPlanSApo 40x 1.25Sil Oil immersion objective (Olympus, Tokyo, Japan) at a resolution of app. 100 µm/pixel (60x) and 600 nm step size. Quantification was performed in individual images after background subtraction with a minimum of 30 cells using ImageJ software. For particle quantification using ImageJ plugin, fluorescent dots with a pixel<sup>2</sup> from 0.1 to 10 and circularity from 0.0 to 1.0 were included in the analysis. The mean dot fluorescence per cell was calculated by dividing the overall intensity of particles with the cellular area in the same field.

### **PSC coefficients analysis and statistics**

For quantification of the co-localization between signals from TOM20/KDEL, TOM20/Lamp1 and Drp1/Tom20, Pearson and Spearman Correlation coefficients (PSC) were calculated by using the PSC co-localization plug-in of ImageJ 1.52e (National Institutes of Health) according to<sup>70</sup>. At least 10 individual cells in three independent images and a minimum of 500 signals were considered for every analysis. Calculated PSC values

were between  $-1$  (negative correlation) and  $+1$  (positive correlation) and the threshold level, under which pixels were treated as background noise, was set at 10. The results were presented as scatter plots with Pearson's and Spearman's coefficients ( $r_p$  and  $r_s$ ).

### **Mitochondria 3D Reconstruction and Morphometric Analysis**

For mitochondrial 3D reconstruction, images were deconvolved using the FIJI plugins point spread function (PSF) generator<sup>71</sup> and DeconvolutionLab<sup>72</sup> (EPFL; <http://bigwww.epfl.ch/>). Z-step was set to 0.6  $\mu\text{m}$  and a PSF algorithm (Born & Wolf 3D Optical model) was used for PSF generation. The generated PSF and a 3D deconvolution algorithm (Richardson-Lucy with TV regularization) were applied to microscopic images using DeconvolutionLab. From the deconvolved 2D and 3D binary images (8-bit images) images, mitochondrial network was determined by generating a skeleton of the images using the Fiji plugin Skeletonize3D and analyzed using the plugin AnalyzeSkeleton (2D/3D). This plugin will tag all pixel/voxels in a skeleton image and then counts the junctions and branches of the mitochondrial network, and measures their average length. For mitochondrial network analysis at least 20 cells were analyzed.

### **Seahorse assays**

Mitochondrial respiration and glycolysis were measured using the Seahorse XFe 24 Analyzer (Agilent, Santa Clara, CA). Therefore 30000 cells/well were plated as a monolayer culture in seahorse cell plates pre-coated with collagen. Oxidative phosphorylation and glycolysis analysis were conducted 2 days after the siRNA KD of Luciferase control or Rab24. To measure *in vivo* mitochondrial respiration, primary hepatocytes were isolated from control or Rab24 KD mice after 5 days of RNAi treatment and directly measured. Mito stress test was performed by injection of 2  $\mu\text{M}$  oligomycin

(Sigma-Aldrich Chemie Munich, Germany), 1  $\mu$ M FCCP (Sigma-Aldrich Chemie Munich, Germany) and 1  $\mu$ M Antimycin A (Sigma-Aldrich Chemie Munich, Germany) + 1  $\mu$ M Rotenone (Sigma-Aldrich Chemie Munich, Germany). To measure oxidative phosphorylation after the block of autophagy, cells were incubated 1 h with 25  $\mu$ M chloroquine prior to the seahorse assay. Glycolysis was measured by additional injection of 100 mM 2-DG (Sigma-Aldrich Chemie Munich, Germany).

### **Cholesterol, bile acid, lactate and FGF21 Secretion**

Dex-free primary hepatocytes in collagen sandwich were washed and starved for 5 hours in Williams E w/o serum 3 days after RNAi. Medium was collected and the amounts of cholesterol, bile acids and FGF21 were determined according to manufacturer's instructions using the Amplex Red Cholesterol Assay Kit (Thermo Fisher Scientific, Waltham, MA), the total bile acid kit from Cell Biolabs (San Diego, CA) and the Mouse/Rat FGF-21 Quantikine ELISA Kit from R & D Systems (Minneapolis, MN) respectively. Lactate concentration was measured with the Lactate Assay kit from Sigma-Aldrich, according to manufacturer's instructions. Amounts of cholesterol, bile acids, lactate and FGF21 were normalized to total protein levels of the cells. Protein levels were obtained using the DC Protein assay kit (BioRad, Hercules, CA).

### **Mitochondrial assays**

Primary hepatocytes cultured for 3 days after RNAi treatment or isolated hepatocytes from control or Rab24 KD mice (5 days post RNAi) were treated for 30 min with 250 nM MitoTracker Red and 200 nM MitoTracker green to determine mitochondrial mass and function, normalized to cell number measured with DAPI fluorescence.

Mitochondrial degradation was assessed using the nucleoid depletion assay<sup>33</sup>. To stimulate mitophagy, 3 days after siRNA treatment primary hepatocytes were incubated with 20  $\mu$ M FCCP for 1 h. After fixation, total DNA and nuclear DNA (DAPI) were stained to determine cytosolic DNA.

Mitophagy was measured by incubating the cells (30000 cells per well in a 96 well plate) with 20  $\mu$ M FCCP alone or with 20  $\mu$ M Chloroquine for 2 h. Accumulation of autophagosomes was measured with the CYTO-ID Autophagy Detection Kit (Enzo, Farmingdale, NY).

### **Autophagy flux**

To determine autophagy flux *in vivo*, control and Rab24 KD mice were either fed ad libitum, starved for 12 h or starved for 12 h + 3 h chloroquine treatment (100 mg/kg). Chloroquine or PBS as control (fed and fasted group) were injected intraperitoneal. Mice were sacrificed simultaneously, liver pieces snap frozen in liquid nitrogen and the concentration of the autophagy markers LC3 and p62 measured via western blot.

Autophagy flux *in vitro* was measured in primary hepatocytes cultured in collagen sandwich 4 days after siRNA treatment. Cells were either kept in full medium, serum and Dex starved for 12 h, or starved 12 h + chloroquine treatment 20  $\mu$ M for 1 h. Cells were either lysed for western blot analysis or fixed in PFA for immunofluorescence.

### **ATP, Ros & Carbonylation assay**

For measuring ATP, Ros production and carbonylation of proteins, 30000 cells per well were cultured in a 96 well plate. 3 days after RNAi concentrations of ATP, Ros and carbonylation were detected using respective kits according to manufacturer's instructions: CellTiter-Fluor Cell Viability Assay (Promega, Madison, WI), DCFDA Cellular ROS

Detection Assay Kit (Abcam, Cambridge, UK) and Protein Carbonyl Content Assay Kit (Abcam, Cambridge, UK) all normalized to cell number measured with DAPI fluorescence.

### **Glucose uptake assay**

Glucose uptake was measured in a 96 well plate containing 30000 cells per well incubated with 10  $\mu$ M 2-NBDG (Thermo Fisher Scientific, Waltham, MA) for 1 h to cells in either basal conditions or supplemented with 2  $\mu$ M Oligomycin, 1  $\mu$ M Antimycin + 1  $\mu$ M Rotenone or 25 mM glucose. Cells were washed twice with PBS and fluorescence of 2-NBDG was measured. 2-NBDG values were normalized to DAPI fluorescence.

### **Statistical analyses and data processing**

Two-tailed, unpaired Student's t-test was performed to calculate statistical significance.  $P < 0.05$  was considered to be statistically significant. Mean  $\pm$  SEM are shown. \* $p < 0.05$ , \*\* $p < 0.01$ , \*\*\* $p < 0.001$ , \*\*\*\* $p < 0.0001$ , \*\*\*\*\*  $p < 0.00001$

### **Reporting Summary**

Further information on research design is available in the Nature Research Reporting Summary linked to this article.

### **Data availability**

Proteomic data generated or analyzed during this study are included in this published article (and its supplementary information files). Additional data that support the findings of this study are available from the corresponding authors on reasonable request.

## **CORRESPONDING AUTHOR**

Correspondence to Anja Zeigerer.

## **ACKNOWLEDGMENTS**

We acknowledge T. Schwarz-Romond, A.M. Cuervo, H.M. McBride, L. Pellegrini, M. Jastroch and L. Scorrano for helpful discussions. We thank A. Takacs, J. Biebl, S. Krämer, Q. Reinold and S. Ambos for mouse care and injections. We thank A. Georgiadi and C. Glantschnig for scientific help. The authors thank N. Itho (Kyoto University Graduate School of Pharmaceutical Sciences, Sakyo, Kyoto, Japan) for providing the FGF21-KO mice. This work was financially supported by DFG Grant ZE1037/1-1, ZE1037/3-1, DZD Grant 920.561-82DZD0032G, EFSD Grant 01KU1501C and BMBF Grant 031L0114A to A.Z., AMPro funding from the Helmholtz Association to S.H., and the DFG within the framework of the Munich Cluster for Systems Neurology (EXC2145 SyNergy) and the Collaborative Research Center (CRC1177) as well as by the Boehringer Ingelheim Foundation to C.B. J.G. was supported by INSERM, the University Cote d'azur and the ANR Young Investigator Program (ANR18-CE14-0035-01-GILLERON). N.K. is funded by Emmy-Noether DFG (KR5166/1-1).

## **AUTHOR CONTRIBUTIONS**

A.Z. designed and directed the project. S.S., G.H., and M.B.D. designed and performed the animal and *in vitro* experiments. Y.K. developed the skeletonization and image analysis of the mitochondrial network. J.J. and C.B. completed the GST-Rab24 pull-down experiments. R.S. performed the triglyceride assays. N.K. and M.M. conducted the proteomics analysis. B.N. performed some western blot analysis. A.L. and S.H. analyzed and blotted the proteomics data and provided information on the MCD-HFD studies. S.G.

and M.R. provided samples of patients with fatty liver disease and NASH and performed the correlation analysis. A.F. for sectioning, staining and quantification of liver tissue K.S. and T.D.M provided the FGF21 KO mice. M.H.d.A. supervised the Rab24 knockout mouse experiments. M.B. provided expression data and correlation analysis of obese patients and patients with type 2 diabetes. J.G. performed the electron microscopy experiments and analysis. A.Z. and S.S. wrote the manuscript. J.G., A.L., C.B., G.H. and S.H. edited the manuscript.

### **COMPETING INTERESTS**

The authors declare no competing interests.

## REFERENCES

- 1 Antonescu, C. N., McGraw, T. E. & Klip, A. Reciprocal regulation of endocytosis and metabolism. *Cold Spring Harbor perspectives in biology* **6**, a016964, doi:10.1101/cshperspect.a016964 (2014).
- 2 Zanoni, P., Velagapudi, S., Yalcinkaya, M., Rohrer, L. & von Eckardstein, A. Endocytosis of lipoproteins. *Atherosclerosis* **275**, 273-295, doi:10.1016/j.atherosclerosis.2018.06.881 (2018).
- 3 Di Fiore, P. P. & von Zastrow, M. Endocytosis, signaling, and beyond. *Cold Spring Harb Perspect Biol* **6**, doi:10.1101/cshperspect.a016865 (2014).
- 4 Wandinger-Ness, A. & Zerial, M. Rab proteins and the compartmentalization of the endosomal system. *Cold Spring Harb Perspect Biol* **6**, a022616, doi:10.1101/cshperspect.a022616 (2014).
- 5 Zeng, J., Feng, S., Wu, B. & Guo, W. Polarized Exocytosis. *Cold Spring Harb Perspect Biol* **9**, doi:10.1101/cshperspect.a027870 (2017).
- 6 Gilleron, J., Gerdes, J. M. & Zeigerer, A. Metabolic regulation through the endosomal system. *Traffic*, doi:10.1111/tra.12670 (2019).
- 7 Bonifacino, J. S. & Glick, B. S. The mechanisms of vesicle budding and fusion. *Cell* **116**, 153-166 (2004).
- 8 Robinson, M. S. Adaptable adaptors for coated vesicles. *Trends in cell biology* **14**, 167-174, doi:10.1016/j.tcb.2004.02.002 (2004).
- 9 Jahn, R. & Scheller, R. H. SNAREs--engines for membrane fusion. *Nature reviews. Molecular cell biology* **7**, 631-643, doi:10.1038/nrm2002 (2006).
- 10 Krahmer, N. *et al.* Organellar Proteomics and Phospho-Proteomics Reveal Subcellular Reorganization in Diet-Induced Hepatic Steatosis. *Dev Cell* **47**, 205-221 e207, doi:10.1016/j.devcel.2018.09.017 (2018).
- 11 Olkkonen, V. M. *et al.* Molecular cloning and subcellular localization of three GTP-binding proteins of the rab subfamily. *J Cell Sci* **106 ( Pt 4)**, 1249-1261 (1993).
- 12 Amaya, C., Militello, R. D., Calligaris, S. D. & Colombo, M. I. Rab24 interacts with the Rab7/RILP complex to regulate endosomal degradation. *Traffic*, doi:10.1111/tra.12431 (2016).
- 13 Rozman, J. *et al.* Identification of genetic elements in metabolism by high-throughput mouse phenotyping. *Nat Commun* **9**, 288, doi:10.1038/s41467-017-01995-2 (2018).
- 14 Zeigerer, A. *et al.* Rab5 is necessary for the biogenesis of the endolysosomal system in vivo. *Nature* **485**, 465-470, doi:10.1038/nature11133 (2012).
- 15 Zeigerer, A. *et al.* Regulation of liver metabolism by the endosomal GTPase Rab5. *Cell Rep* **11**, 884-892, doi:10.1016/j.celrep.2015.04.018 (2015).
- 16 Koliaki, C. *et al.* Adaptation of hepatic mitochondrial function in humans with non-alcoholic fatty liver is lost in steatohepatitis. *Cell Metab* **21**, 739-746, doi:10.1016/j.cmet.2015.04.004 (2015).
- 17 Gilleron, J. *et al.* Image-based analysis of lipid nanoparticle-mediated siRNA delivery, intracellular trafficking and endosomal escape. *Nat Biotechnol* **31**, 638-646, doi:10.1038/nbt.2612 (2013).

- 18 Zeigerer, A. *et al.* Functional properties of hepatocytes in vitro are correlated with cell polarity maintenance. *Exp Cell Res* **350**, 242-252, doi:10.1016/j.yexcr.2016.11.027 (2017).
- 19 Niopek, K. *et al.* A Hepatic GAbp-AMPK Axis Links Inflammatory Signaling to Systemic Vascular Damage. *Cell Rep* **20**, 1422-1434, doi:10.1016/j.celrep.2017.07.023 (2017).
- 20 Schrepfer, E. & Scorrano, L. Mitofusins, from Mitochondria to Metabolism. *Mol Cell* **61**, 683-694, doi:10.1016/j.molcel.2016.02.022 (2016).
- 21 Gomes, L. C., Di Benedetto, G. & Scorrano, L. During autophagy mitochondria elongate, are spared from degradation and sustain cell viability. *Nat Cell Biol* **13**, 589-598, doi:10.1038/ncb2220 (2011).
- 22 Jheng, H. F. *et al.* Mitochondrial fission contributes to mitochondrial dysfunction and insulin resistance in skeletal muscle. *Mol Cell Biol* **32**, 309-319, doi:10.1128/MCB.05603-11 (2012).
- 23 Picard, M., White, K. & Turnbull, D. M. Mitochondrial morphology, topology, and membrane interactions in skeletal muscle: a quantitative three-dimensional electron microscopy study. *J Appl Physiol (1985)* **114**, 161-171, doi:10.1152/jappphysiol.01096.2012 (2013).
- 24 Pernas, L. & Scorrano, L. Mito-Morphosis: Mitochondrial Fusion, Fission, and Cristae Remodeling as Key Mediators of Cellular Function. *Annu Rev Physiol* **78**, 505-531, doi:10.1146/annurev-physiol-021115-105011 (2016).
- 25 Tonachini, L. *et al.* Chondrocyte protein with a poly-proline region (CHPPR) is a novel mitochondrial protein and promotes mitochondrial fission. *J Cell Physiol* **201**, 470-482, doi:10.1002/jcp.20126 (2004).
- 26 Monticone, M. *et al.* The nuclear genes Mtf1 and Duf1 regulate mitochondrial dynamic and cellular respiration. *J Cell Physiol* **225**, 767-776, doi:10.1002/jcp.22279 (2010).
- 27 Abrams, A. J. *et al.* Mutations in SLC25A46, encoding a UGO1-like protein, cause an optic atrophy spectrum disorder. *Nat Genet* **47**, 926-932, doi:10.1038/ng.3354 (2015).
- 28 Friedman, J. R. *et al.* ER tubules mark sites of mitochondrial division. *Science* **334**, 358-362, doi:10.1126/science.1207385 (2011).
- 29 Korobova, F., Ramabhadran, V. & Higgs, H. N. An actin-dependent step in mitochondrial fission mediated by the ER-associated formin INF2. *Science* **339**, 464-467, doi:10.1126/science.1228360 (2013).
- 30 Smirnova, E., Griparic, L., Shurland, D. L. & van der Bliek, A. M. Dynamin-related protein Drp1 is required for mitochondrial division in mammalian cells. *Mol Biol Cell* **12**, 2245-2256, doi:10.1091/mbc.12.8.2245 (2001).
- 31 Gomes, L. C. & Scorrano, L. High levels of Fis1, a pro-fission mitochondrial protein, trigger autophagy. *Biochim Biophys Acta* **1777**, 860-866, doi:10.1016/j.bbabi.2008.05.442 (2008).
- 32 Twig, G. *et al.* Fission and selective fusion govern mitochondrial segregation and elimination by autophagy. *EMBO J* **27**, 433-446, doi:10.1038/sj.emboj.7601963 (2008).
- 33 Lazarou, M. *et al.* The ubiquitin kinase PINK1 recruits autophagy receptors to induce mitophagy. *Nature* **524**, 309-314, doi:10.1038/nature14893 (2015).

- 34 Sun, N. *et al.* Measuring In Vivo Mitophagy. *Mol Cell* **60**, 685-696, doi:10.1016/j.molcel.2015.10.009 (2015).
- 35 Munafo, D. B. & Colombo, M. I. Induction of autophagy causes dramatic changes in the subcellular distribution of GFP-Rab24. *Traffic* **3**, 472-482 (2002).
- 36 Madrigal-Matute, J. & Cuervo, A. M. Regulation of Liver Metabolism by Autophagy. *Gastroenterology* **150**, 328-339, doi:10.1053/j.gastro.2015.09.042 (2016).
- 37 Klionsky, D. J. *et al.* Guidelines for the use and interpretation of assays for monitoring autophagy in higher eukaryotes. *Autophagy* **4**, 151-175, doi:10.4161/auto.5338 (2008).
- 38 Stolz, A., Ernst, A. & Dikic, I. Cargo recognition and trafficking in selective autophagy. *Nat Cell Biol* **16**, 495-501, doi:10.1038/ncb2979 (2014).
- 39 Sha, Z., Schnell, H. M., Ruoff, K. & Goldberg, A. Rapid induction of p62 and GABARAPL1 upon proteasome inhibition promotes survival before autophagy activation. *J Cell Biol* **217**, 1757-1776, doi:10.1083/jcb.201708168 (2018).
- 40 Yla-Anttila, P. *et al.* RAB24 facilitates clearance of autophagic compartments during basal conditions. *Autophagy* **11**, 1833-1848, doi:10.1080/15548627.2015.1086522 (2015).
- 41 Matsumoto, M. *et al.* An improved mouse model that rapidly develops fibrosis in non-alcoholic steatohepatitis. *Int J Exp Pathol* **94**, 93-103, doi:10.1111/iep.12008 (2013).
- 42 Itagaki, H., Shimizu, K., Morikawa, S., Ogawa, K. & Ezaki, T. Morphological and functional characterization of non-alcoholic fatty liver disease induced by a methionine-choline-deficient diet in C57BL/6 mice. *Int J Clin Exp Pathol* **6**, 2683-2696 (2013).
- 43 Perry, R. J. *et al.* Reversal of hypertriglyceridemia, fatty liver disease, and insulin resistance by a liver-targeted mitochondrial uncoupler. *Cell Metab* **18**, 740-748, doi:10.1016/j.cmet.2013.10.004 (2013).
- 44 Perry, R. J., Zhang, D., Zhang, X. M., Boyer, J. L. & Shulman, G. I. Controlled-release mitochondrial protonophore reverses diabetes and steatohepatitis in rats. *Science* **347**, 1253-1256, doi:10.1126/science.aaa0672 (2015).
- 45 Sood, A. *et al.* A Mitofusin-2-dependent inactivating cleavage of Opa1 links changes in mitochondria cristae and ER contacts in the postprandial liver. *Proc Natl Acad Sci U S A* **111**, 16017-16022, doi:10.1073/pnas.1408061111 (2014).
- 46 Gomes, L. C. & Scorrano, L. Mitochondrial morphology in mitophagy and macroautophagy. *Biochim Biophys Acta* **1833**, 205-212, doi:10.1016/j.bbamcr.2012.02.012 (2013).
- 47 Gonzalez-Rodriguez, A. *et al.* Impaired autophagic flux is associated with increased endoplasmic reticulum stress during the development of NAFLD. *Cell Death Dis* **5**, e1179, doi:10.1038/cddis.2014.162 (2014).
- 48 Yang, L., Li, P., Fu, S., Calay, E. S. & Hotamisligil, G. S. Defective hepatic autophagy in obesity promotes ER stress and causes insulin resistance. *Cell Metab* **11**, 467-478, doi:10.1016/j.cmet.2010.04.005 (2010).
- 49 Zorzano, A., Liesa, M. & Palacin, M. Role of mitochondrial dynamics proteins in the pathophysiology of obesity and type 2 diabetes. *Int J Biochem Cell Biol* **41**, 1846-1854, doi:10.1016/j.biocel.2009.02.004 (2009).

- 50 Duraisamy, A. J., Mohammad, G. & Kowluru, R. A. Mitochondrial fusion and maintenance of mitochondrial homeostasis in diabetic retinopathy. *Biochim Biophys Acta Mol Basis Dis*, doi:10.1016/j.bbadis.2019.03.013 (2019).
- 51 Ayanga, B. A. *et al.* Dynamin-Related Protein 1 Deficiency Improves Mitochondrial Fitness and Protects against Progression of Diabetic Nephropathy. *J Am Soc Nephrol* **27**, 2733-2747, doi:10.1681/ASN.2015101096 (2016).
- 52 Wang, Q. *et al.* Metformin Suppresses Diabetes-Accelerated Atherosclerosis via the Inhibition of Drp1-Mediated Mitochondrial Fission. *Diabetes* **66**, 193-205, doi:10.2337/db16-0915 (2017).
- 53 Kandimalla, R. *et al.* Reduced dynamin-related protein 1 protects against phosphorylated Tau-induced mitochondrial dysfunction and synaptic damage in Alzheimer's disease. *Hum Mol Genet* **25**, 4881-4897, doi:10.1093/hmg/ddw312 (2016).
- 54 Larance, M. *et al.* Characterization of the role of the Rab GTPase-activating protein AS160 in insulin-regulated GLUT4 trafficking. *J Biol Chem* **280**, 37803-37813, doi:10.1074/jbc.M503897200 (2005).
- 55 Sano, H. *et al.* Rab10, a target of the AS160 Rab GAP, is required for insulin-stimulated translocation of GLUT4 to the adipocyte plasma membrane. *Cell Metab* **5**, 293-303, doi:10.1016/j.cmet.2007.03.001 (2007).
- 56 Vassilopoulos, S. *et al.* A role for the CHC22 clathrin heavy-chain isoform in human glucose metabolism. *Science* **324**, 1192-1196, doi:10.1126/science.1171529 (2009).
- 57 Bartuzi, P. *et al.* CCC- and WASH-mediated endosomal sorting of LDLR is required for normal clearance of circulating LDL. *Nat Commun* **7**, 10961, doi:10.1038/ncomms10961 (2016).
- 58 Fedoseienko, A. *et al.* The COMMD Family Regulates Plasma LDL Levels and Attenuates Atherosclerosis Through Stabilizing the CCC Complex in Endosomal LDLR Trafficking. *Circ Res* **122**, 1648-1660, doi:10.1161/CIRCRESAHA.117.312004 (2018).
- 59 Kloting, N. *et al.* Insulin-sensitive obesity. *Am J Physiol Endocrinol Metab* **299**, E506-515, doi:10.1152/ajpendo.00586.2009 (2010).
- 60 Bluher, M., Unger, R., Rassoul, F., Richter, V. & Paschke, R. Relation between glycaemic control, hyperinsulinaemia and plasma concentrations of soluble adhesion molecules in patients with impaired glucose tolerance or Type II diabetes. *Diabetologia* **45**, 210-216, doi:10.1007/s00125-001-0723-3 (2002).
- 61 Apostolopoulou, M. *et al.* Specific Hepatic Sphingolipids Relate to Insulin Resistance, Oxidative Stress, and Inflammation in Nonalcoholic Steatohepatitis. *Diabetes Care* **41**, 1235-1243, doi:10.2337/dc17-1318 (2018).
- 62 Rink, J., Ghigo, E., Kalaidzidis, Y. & Zerial, M. Rab conversion as a mechanism of progression from early to late endosomes. *Cell* **122**, 735-749, doi:10.1016/j.cell.2005.06.043 (2005).
- 63 Wincott, F. *et al.* Synthesis, deprotection, analysis and purification of RNA and ribozymes. *Nucleic Acids Res* **23**, 2677-2684 (1995).
- 64 Kulak, N. A., Pichler, G., Paron, I., Nagaraj, N. & Mann, M. Minimal, encapsulated proteomic-sample processing applied to copy-number estimation in eukaryotic cells. *Nat Methods* **11**, 319-324, doi:10.1038/nmeth.2834 (2014).

- 65 Vitale, G. *et al.* Distinct Rab-binding domains mediate the interaction of Rabaptin-5 with GTP-bound Rab4 and Rab5. *EMBO J* **17**, 1941-1951, doi:10.1093/emboj/17.7.1941 (1998).
- 66 Feuchtinger, A. *et al.* Image analysis of immunohistochemistry is superior to visual scoring as shown for patient outcome of esophageal adenocarcinoma. *Histochem Cell Biol* **143**, 1-9, doi:10.1007/s00418-014-1258-2 (2015).
- 67 Zellmer, S. *et al.* Transcription factors ETF, E2F, and SP-1 are involved in cytokine-independent proliferation of murine hepatocytes. *Hepatology* **52**, 2127-2136, doi:10.1002/hep.23930 (2010).
- 68 Godoy, P. *et al.* Recent advances in 2D and 3D in vitro systems using primary hepatocytes, alternative hepatocyte sources and non-parenchymal liver cells and their use in investigating mechanisms of hepatotoxicity, cell signaling and ADME. *Arch Toxicol* **87**, 1315-1530, doi:10.1007/s00204-013-1078-5 (2013).
- 69 Mollica, M. P. *et al.* Butyrate Regulates Liver Mitochondrial Function, Efficiency, and Dynamics in Insulin-Resistant Obese Mice. *Diabetes* **66**, 1405-1418, doi:10.2337/db16-0924 (2017).
- 70 French, A. P., Mills, S., Swarup, R., Bennett, M. J. & Pridmore, T. P. Colocalization of fluorescent markers in confocal microscope images of plant cells. *Nat Protoc* **3**, 619-628, doi:10.1038/nprot.2008.31 (2008).
- 71 Kirshner, H., Aguet, F., Sage, D. & Unser, M. 3-D PSF fitting for fluorescence microscopy: implementation and localization application. *J Microsc* **249**, 13-25, doi:10.1111/j.1365-2818.2012.03675.x (2013).
- 72 Sage, D. *et al.* DeconvolutionLab2: An open-source software for deconvolution microscopy. *Methods* **115**, 28-41, doi:10.1016/j.ymeth.2016.12.015 (2017).

## FIGURE LEGENDS

### Figure 1: *RAB24* was upregulated in NAFLD patients and regulated glucose tolerance and serum lipid parameters in mice.

Relative expression of *RAB24* in liver of obese patients (**a**) and patients with NAFLD +/- steatosis and NASH (**b**) versus healthy controls. (**c**) ipGTT (2 g/kg) and area under the curve (AUC) (**d**) after 6 h starvation on day 5 after RNAi (N=6 animals). (**e**) Representative Western blots for Akt in muscle of insulin-injected mice (0.75U/kg, 7 min) after 6 h fasting and quantification thereof in (**f**). The experiment was done twice with similar results. (**g**) FGF21 expression and secretion (**i**) in primary hepatocytes after 3 days of KD. 12 wells pooled into N=4 replicates for (**g**). N=12 wells per condition in (**i**). (**h**) FGF21 expression in liver (N=10 (CTR) and N=12 (KD) animals) and amounts in serum (**j**) (N=6 (CTR) and N=8 (KD) animals) after 6 days of RNAi. ipGTT of heterozygous (**k**) (N=8 animals) and homozygous (**l**) (N=9 animals) FGF21 KO mice after 5 days of RNAi. Representative Western blots for Akt in muscle of insulin-injected heterozygous (**m**) and homozygous (**o**) FGF21 KO mice (0.75U/kg, 7 min) after 6 h fasting and quantification thereof in (**n**) and (**p**), respectively. (**q**) Representative confocal images (maximal projection of 3 slices) of primary hepatocytes internalizing DiI-LDL (grey) for 60 min stained with dapi and quantification thereof with Fiji in (**r**). The images are representative of three independent wells of a 24-well plate. The experiment was repeated twice with similar results. Scale bar 20  $\mu$ m. (**s**) Cholesterol secretion assay in primary hepatocytes after 4 days of KD from N=11 wells per condition. (**t**) Liver bile acids after 6 days of RNAi (N=6 animals). All animals treated with control (CTR) and Rab24 (KD) LNPs (0.5 mg/kg) (N=3 (**e**, **f**, **m-p**) animals per condition). Primary hepatocytes treated with control (CTR) or Rab24 (KD) siRNA (40 nM) (mean +/- SEM). \*P<0.05, \*\*P<0.01, \*\*\*P<0.001, \*\*\*\*P<0.0001, by two-tailed unpaired Student's t-test. Only data that reached statistical significance are indicated.

**Figure 2: Liver specific KD of Rab24 induced an up-regulation of mitochondrial proteins.** (a) Log<sub>2</sub> fold changes of protein abundance upon KD of Rab24 in wild type mice under chow diet with corresponding significance values from N=6 animals per condition. Differentially abundant proteins (N=622) (p-value <0.05) upon Rab24KD are indicated (red – up (N=287) and blue – down (N=335)). Significantly up-or-downregulated proteins were determined by Student's t-test (FDR 0.05). (b, c) Proteins regulated by Rab24KD were subjected to functional enrichment analyses. A modified Fisher Exact test (Ease Score) is used for the functional enrichment analyses. p-values are corrected for multiple testing using the Benjamini-Hochberg (FDR) Method. Significantly enriched pathways (FDR<0.1) are shown for KEGG Pathways (b) and GO cellular component ontology (c). (d) Prohibitin staining from liver sections of control and Rab24KD mice and quantification thereof in (e). The images are representative of six independent biological replicates. All measured after 6 days of KD of Rab24 with LNPs (0.5mg/kg). (mean +/- SEM) \*\*\*\*P<0.0001 by two-tailed unpaired Student's t-test.

**Figure 3. Rab24 depletion led to an increase in mitochondrial mass and function.**

Representative confocal images (single confocal section) of primary hepatocytes (a) and liver sections (b) stained with dapi, phalloidin (green) and Tom20 (grey) and quantification thereof with Fiji in (c) and (d) after 3 or 6 days of RNAi treatment. The images are representative of three independent wells of a 24-well plate (a) or of four independent biological samples (b). Quantifications are derived from N=33 (CTR) and N=25 (KD) for (c) and N=9 (CTR) and N=12 (KD) for (d) cellular regions. Staining of Mitotracker Green (200 nM for 45 min) in primary hepatocytes after 3 days of RNAi *in vitro* (e) (N=12 wells per condition) and in hepatocytes isolated after *in vivo* RNAi for 5 days (f) (N=32 wells per

condition) normalized to dapi. Seahorse measurements of the oxygen consumption rate (OCR) and their corresponding metabolic rates after 3 days of KD in primary hepatocytes *in vitro* (**g, h**) and in hepatocytes isolated after *in vivo* RNAi for 5 days (**i, j**) (N=10 wells per condition for **g** and **i**, except N=7 for CTR *in vivo*). N=3 time points with 10 wells/time point (basal and ATP production) in **h** and **j**. N=8 (CTR) and N=9 (KD) in (**h**), N=6 (CTR) and N=10 (KD) in (**j**) wells per condition for maximal respiration. The experiment was repeated five times with similar results. Staining of Mitotracker Red (250 nM for 45 min) in primary hepatocytes after 3 days of RNAi *in vitro* (**k**) (N=12 wells per condition) and in hepatocytes isolated after *in vivo* RNAi for 5 days (**l**) (N=32 wells per condition) normalized to dapi. (**m, n, o**) levels of ATP, ROS and carbonylation of proteins, respectively (N=18 (**m**), N=6 (**n**) and N=3 (**o**) wells per condition). All animals treated with control (CTR) and Rab24 (KD) LNPs (0.5 mg/kg). Primary hepatocytes treated with control (CTR) or Rab24 (KD) siRNA (40 nM) and measured after 3 days after RNAi (mean +/- SEM). \*P<0.05, \*\*P<0.01, \*\*\*\*P<0.0001, \*\*\*\*\*P<0.00001 by two-tailed unpaired Student's t-test.

**Figure 4: Rab24 KD increased mitochondrial area and connectivity.**

(**a**) Electron micrographs of mitochondria and quantification of mitochondria morphology by morpho-EM for density (**b**), surface area (**c**), perimeter or contour (**d**), form factor or complexity (**e**) and circularity (**f**) of control and Rab24KD livers. (N=30 cells for **b**, N=700-1000 mitochondria for **c-f**). The images are representative of 4 independent biological replicates. Scale bar 2  $\mu$ m. Representative confocal images (single confocal section) of liver sections from control (**g**) and Rab24KD (**h**) stained with dapi (blue), phalloidin (green) and Tom20 (grey) of single section, deconvolved, zoomed and skeletonized with Fiji. The images are representative of N=3 (CTR) and N=4 (KD)

independent biological samples, which give rise to the quantifications in **i-k**. (**i**, **j**, **k**) quantification of number of branches, numbers of junctions per area and mean length of the branches with Fiji. Scale bar 20  $\mu$ m. All animals treated with control (CTR) and Rab24 (KD) LNPs (0.5 mg/kg). \* $P < 0.05$ , \*\*\*\* $P < 0.0001$ , \*\*\*\*\* $P < 0.00001$  by two-tailed unpaired Student's t-test.

**Figure 5: Rab24 KD increases mitochondria connectivity by interfering with the fission machinery.**

Representative confocal images (single confocal section) of primary hepatocytes stained with dapi (blue), FIS1 (**a**) and DRP1 (**b**) in grey and quantification thereof with Fiji in (**c**) from N=45 (CTR) and N=51 (KD) individual cells. The images are representative of three independent wells of a 24-well plate. The experiment was repeated twice with similar results. (**d**) Abundance of DRP1/Dnml1 in the liver by proteomics from N=6 animals per condition. (**e**) Representative confocal images (single confocal section) of primary hepatocytes stained with dapi (blue), Tom20 (green) and Drp1 (red). The images are representative of three independent wells of a 24-well plate. The experiment was repeated twice with similar results. Person's and Spearman's correlation analyzed with Fiji representing overlap between the green and red channel in (**f**) from 3 wells per condition. All measured after 3 days of RNAi (40 nM) in primary hepatocytes (mean +/- SEM). Scale bar 20  $\mu$ m. (**g**) Pulldown assay for Fis1 and Drp1 with Rab24 or Rab3a as control in mice fasted for 12 h or fasted and refed for 2h. N=3 mice per condition. The experiment was done twice with similar results. \*\*\* $P < 0.001$ , \*\*\*\* $P < 0.0001$  by two-tailed unpaired Student's t-test. Only data that reached statistical significance are indicated.

**Figure 6: Rab24KD causes a reduction in mitophagy and an increase in autophagic flux**

(a) Representative confocal images (single section) of primary hepatocytes stained for total DNA and dapi to assess cytosolic mtDNA under basal conditions and after 1 h of FCCP (20  $\mu$ M) treatment. Scale bar 40  $\mu$ m. The images are representative of three independent wells of a 24-well plate. The experiment was done twice with similar results. (b) Quantification of basal, FCCP and oligomycin (10  $\mu$ M) treated hepatocytes with Fiji from N=13 (CTR-basal), N=15 (CTR-FCCP), N=14 (CTR-oligomycin), N=14 (KD-basal and FCCP) and N=12 (KD-oligomycin) cellular regions. (c) Electron micrographs of mitophagic events and quantification thereof in (d). Red arrows indicate mitophagic events. Scale bar 2  $\mu$ m. N=6 wells per condition. (e) Representative Western blots of LC3-II/VCP levels in primary hepatocytes (*in vitro*) and liver tissue (*in vivo*) in fed, starved or chloroquine treated conditions. Cells were kept in full medium (fed) or serum starved for 12 h (fasted), followed by 20  $\mu$ M chloroquine treatment for 3 h (fasted & CQ). Mice were either fed ad libitum, fasted for 12 h, or fasted for 12 hours followed by 100 mg/kg chloroquine treatment for 3 h (fasted & CQ). LC3-II flux (fasted&CQ/fast) and net flux (fasted&CQ-fast) measurements of LC3-II protein levels in primary hepatocytes (f) and liver tissue (g). The quantifications in (f) are from six independent wells of a 24-well plate pooled into N=2 replicates. All animals treated with control (CTR) and Rab24 (KD) LNPs (0.5 mg/kg) for 5 days (N=2 animals per condition). Both experiments were done twice with similar results. (h) Representative confocal images (3 merged middle sections) of primary hepatocytes stained for LC3-II and treated as described in (e). Scale bar 30  $\mu$ m. The images are representative of three independent wells of a 24-well plate. Quantification of LC3-II flux (i) and net flux (j) in hepatocytes acquired in (h) from N=22 (CTR-flux and net flux), N=19 (KD-flux), N=20 (KD-net flux) cells per condition. Primary hepatocytes treated with

control (CTR) or Rab24 (KD) siRNA (40 nM) and measured 3 days after RNAi (mean +/- SEM). \*P<0.05, \*\*P<0.01, \*\*\*\*P<0.0001 by two-tailed unpaired Student's t-test.

**Figure 7: Depletion of Rab24 in high fat diet fed mice improved serum lipid and glucose parameters.**

Serum parameters for total Cholesterol (a), LDL (b), ApoB (c) and ALT (d). N=4 (LFD), N=5 (HFD-CTR) and N=6 (HFD-KD) animals analyzed. (e) H&E staining of LFD control, HFD control and HFD Rab24 KD liver sections and quantification thereof for hepatic lipid accumulations (% steatosis) (f). Scale bar 200  $\mu$ m. The images are representative of five (LFD) or six (HFD) independent biological samples, which result in the quantification in f. The experiment was done twice with similar results. (g) Triglyceride content of livers of HFD control and HFD Rab24 KD mice (N=7 animals per condition). (h) Liver/body weight ratio of LFD control (N=5), HFD control (N=6) and HFD Rab24 KD (N=6) mice. All measured after 14 days of KD with LNPs (weekly injection; 0.5 mg/kg) and 6 h starvation in 15-week HFD mice. Fasted blood glucose levels (i) in LFD control (N=6), HFD control (N=5) and HFD Rab24 KD (N=5) mice. ipGTT (2 g/kg) (j) and its area under the curve (k) after 4 weeks of KD with LNPs (weekly injection; 0.5 mg/kg) in 17-week HFD mice. (mean +/- SEM; N=12 (CTR) and N=10 (KD) animals per condition). (l) Representative confocal images (maximal projection of 3 merged confocal sections) of 15-week HFD livers stained for Tom20 (magenta) and dapi and quantification thereof in (m). Scale bar 20  $\mu$ m. The images are representative of three independent biological samples. The experiment was done twice with similar results. (n) Seahorse measurements of the OCR rates after KD upon oleate and palmitate treatment (N=3 time points with 3 wells/time point) after 3 days after RNAi (40 nM) in primary hepatocytes (mean +/- SEM). \*P<0.05, \*\*P<0.01, \*\*\*P<0.001, \*\*\*\*P<0.00001 by two-tailed unpaired Student's t-test.

**Figure 8: KD of Rab24 in a NASH mouse model ameliorates liver steatosis and inflammation**

(a) Relative expression of Rab24 in the livers of LFD control, MCD-HFD control and Rab24KD mice. (b) Body weight, (c) blood glucose levels, (d) liver to body weight ratio, H&E staining (e) and their quantification for hepatic lipid accumulations (% steatosis) (f) of LFD control, MCD-HFD control and MCD-HFD Rab24 KD livers. Scale bar 500  $\mu$ m. The images are representative of six independent biological samples. The experiment was done twice with similar results. (g) Triglyceride content, serum ALT levels (h) and relative expression of early NASH markers (i, j) in the livers of LFD control, MCD control and MCD Rab24 KD mice. All measured after 4 weeks of MCD diet and simultaneous KD with LNPs (weekly injection; 0.5 mg/kg) and 6 h starvation. (mean  $\pm$  SEM; N=4 (b, c), N=5 LFD-CTR (a, h, j), N=6 MCD-HFD (a, h, j), N=6 (a, d, f-j) animals per condition). \*P<0.05, \*\*P<0.01, \*\*\*P<0.001, \*\*\*\*P<0.0001 by two-tailed unpaired Student's t-test.

**Table 1.** Serum metabolic parameters of Rab24KD in wildtyp chow fed mice. N=6 aminlas per condition. Mean +/- SEM by two-tailed unpaired Student's t-test.

<b>Parameters</b>	<b>Control</b>	<b>Rab24 KD</b>	<b>p-value</b>
Albumin (g/L)	29.98 ± 0.49	28.43 ± 1.68	0.362
ALT (U/L)	34.25 ± 4.24	48.88 ± 13.85	0.336
Apo A (g/L)	0.24 ± 0.003	0.23 ± 0.01	0.112
Apo B (mg/dl)	0.08 ± 0.005	0.07 ± 0.003	<b>0.018</b>
AST (U/L)	223.33 ± 44.40	277.00 ± 46.94	0.426
Cholesterol (mg/dl)	107.83 ± 2.37	89.17 ± 6.44	<b>0.022</b>
HDL (mg/dl)	73.35 ± 1.84	66.03 ± 2.90	0.059
LDH (U/L)	1128.00 ± 221.71	955.33 ± 68.08	0.474
LDL (mg/dl)	21.63 ± 1.1	15.92 ± 0.79	<b>0.002</b>
Total protein (g/dl)	54.26 ± 0.41	51.64 ± 2.52	0.288
Triglycerides (mg/dl)	101.17 ± 4.82	94.17 ± 6.11	0.389

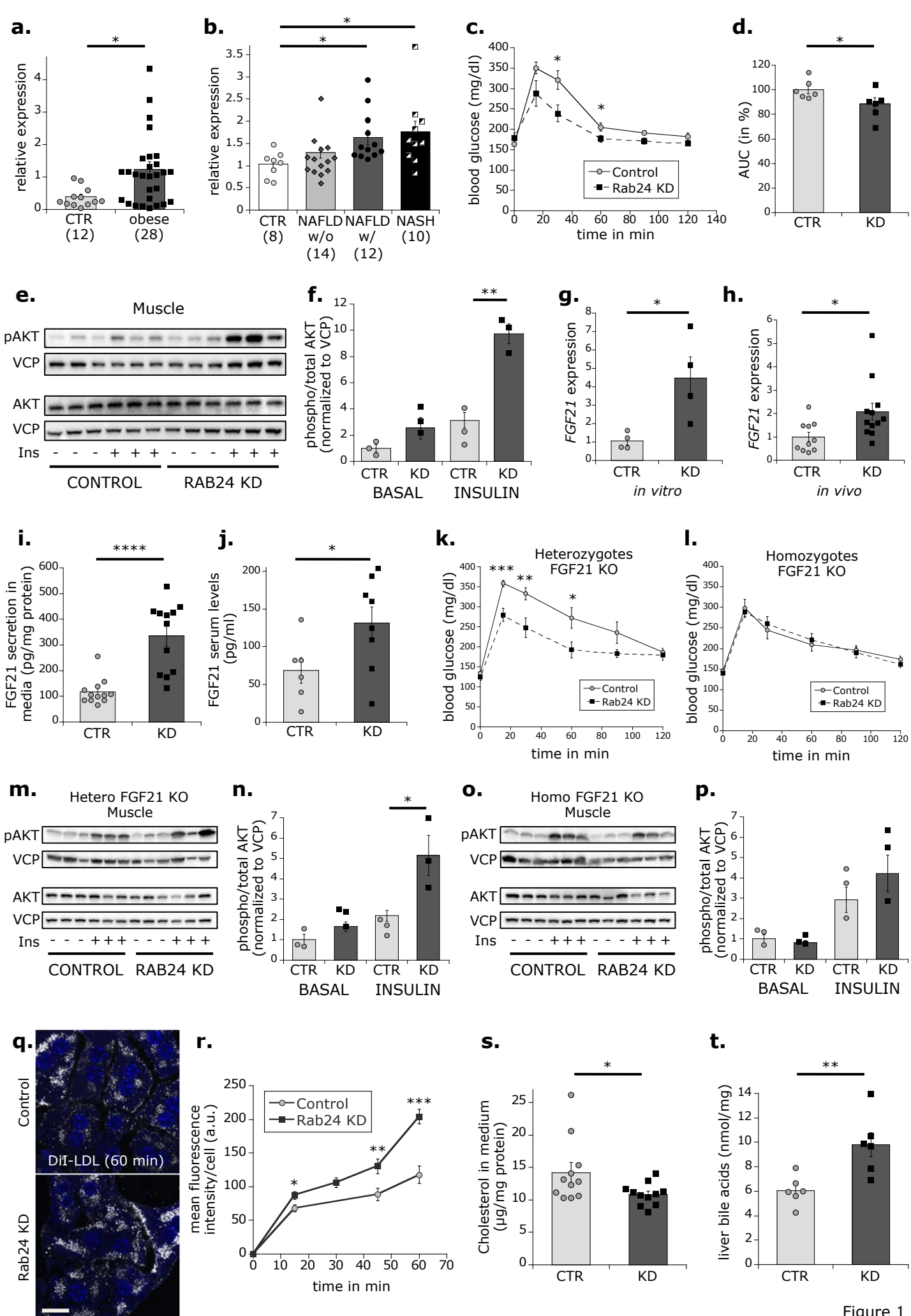


Figure 1

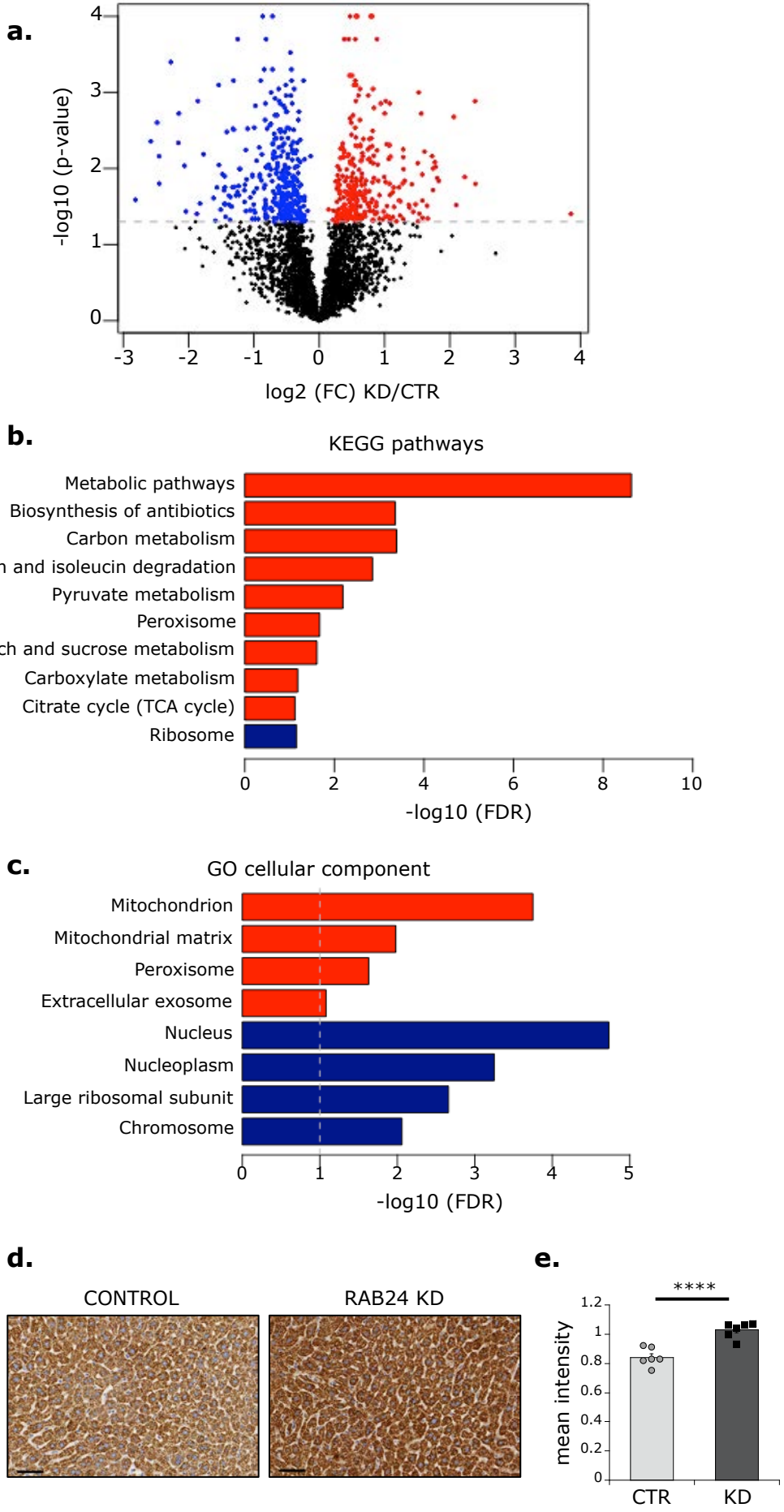


Figure 2

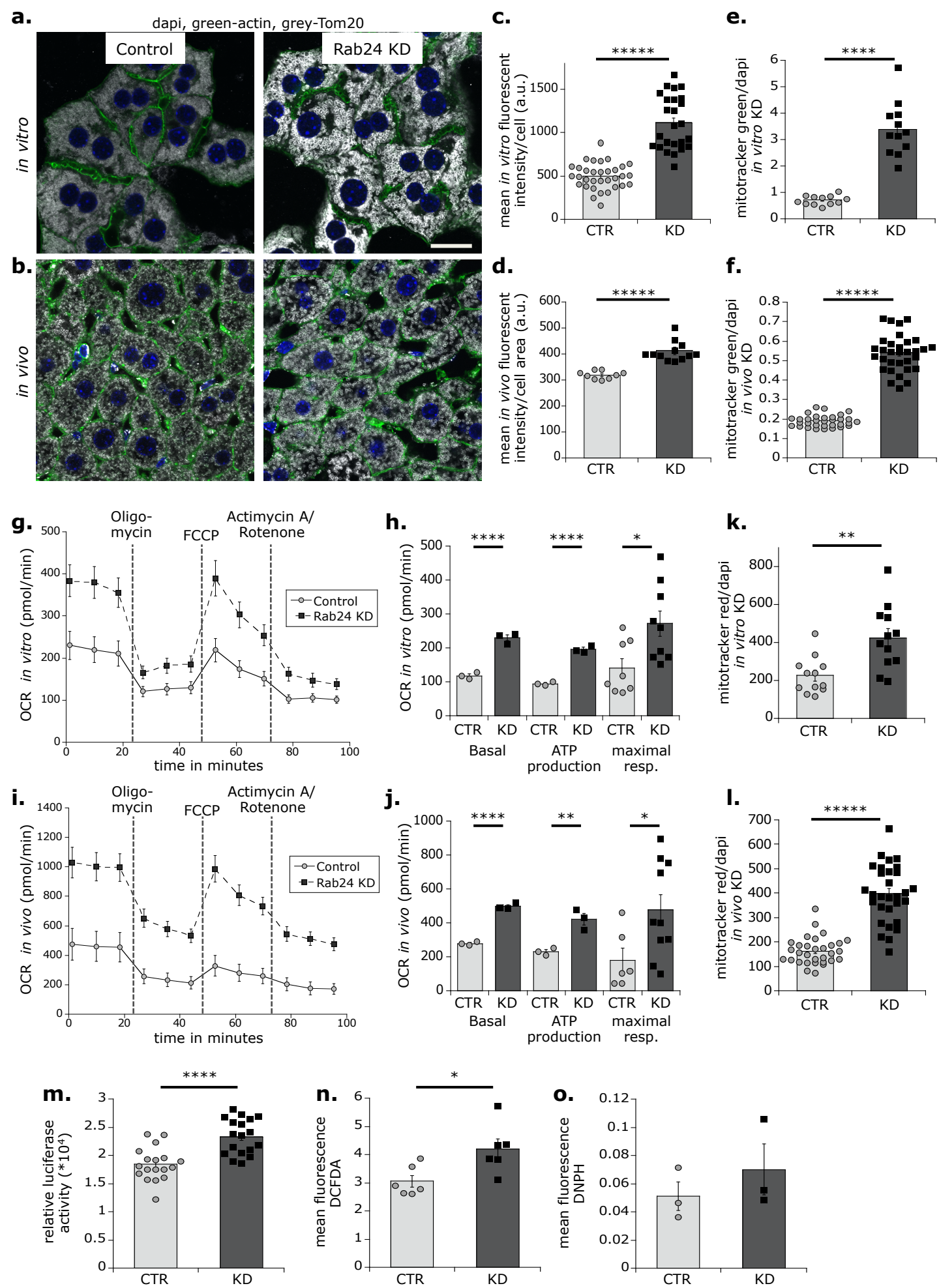


Figure 3

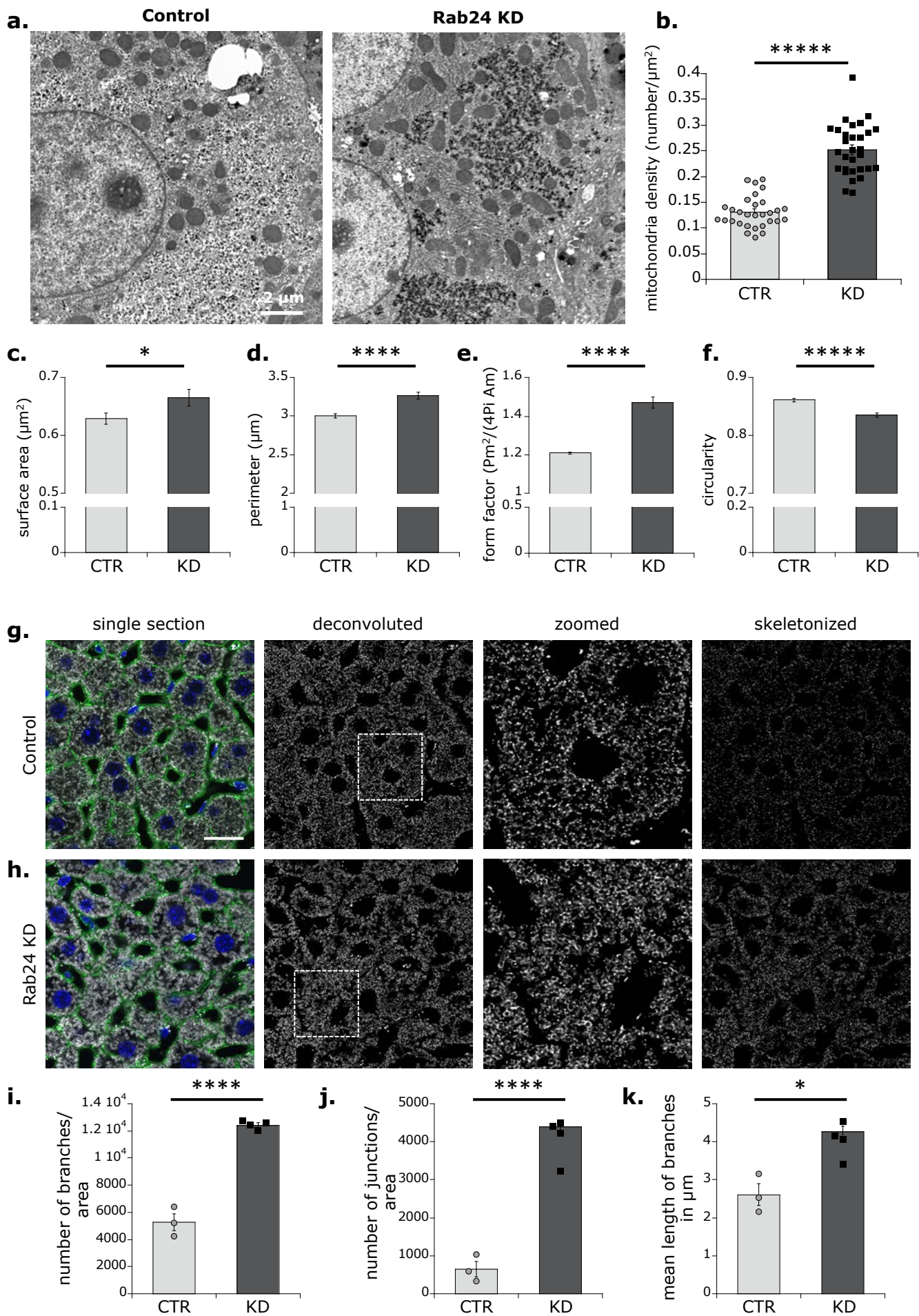


Figure 4

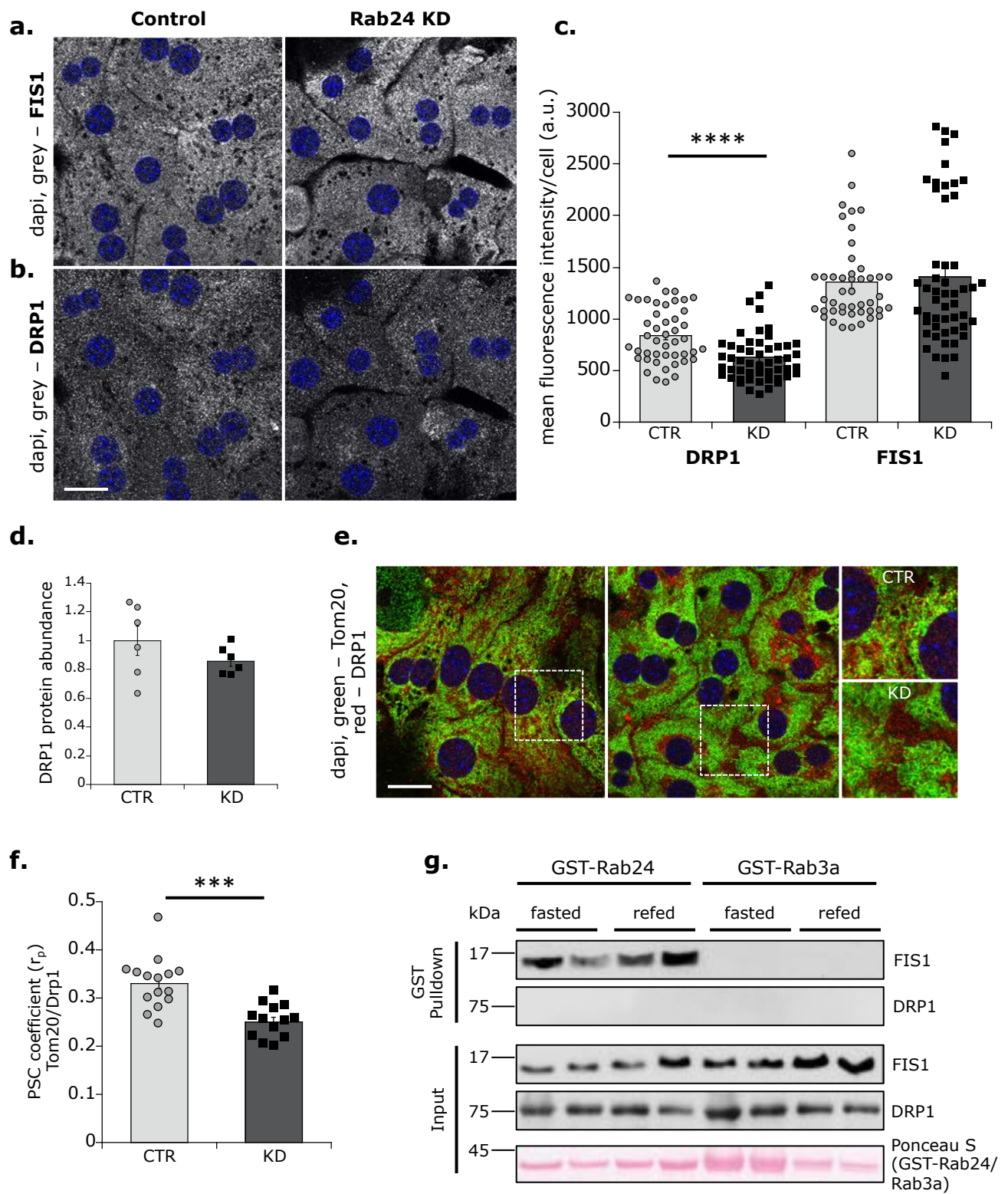


Figure 5

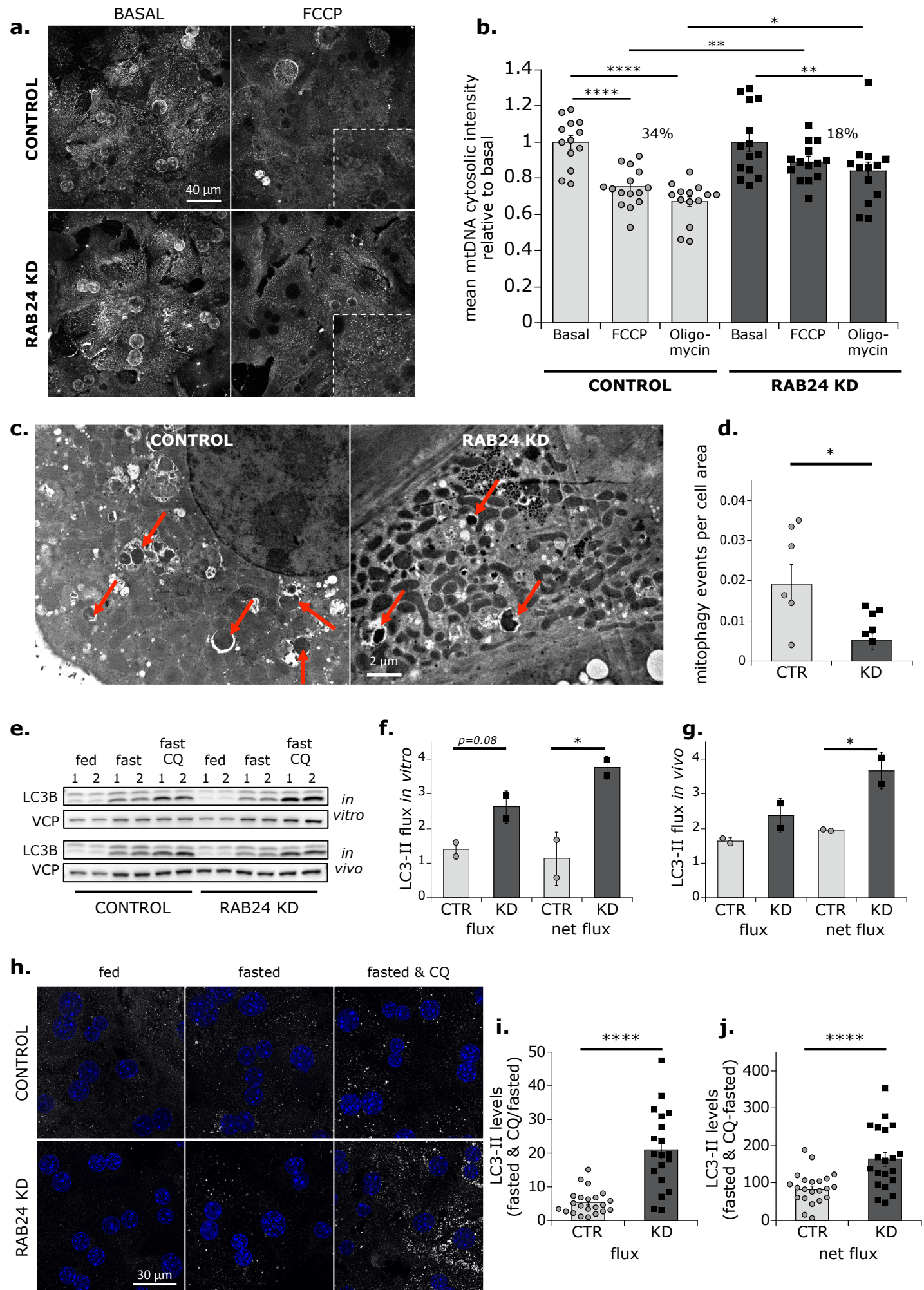


Figure 6

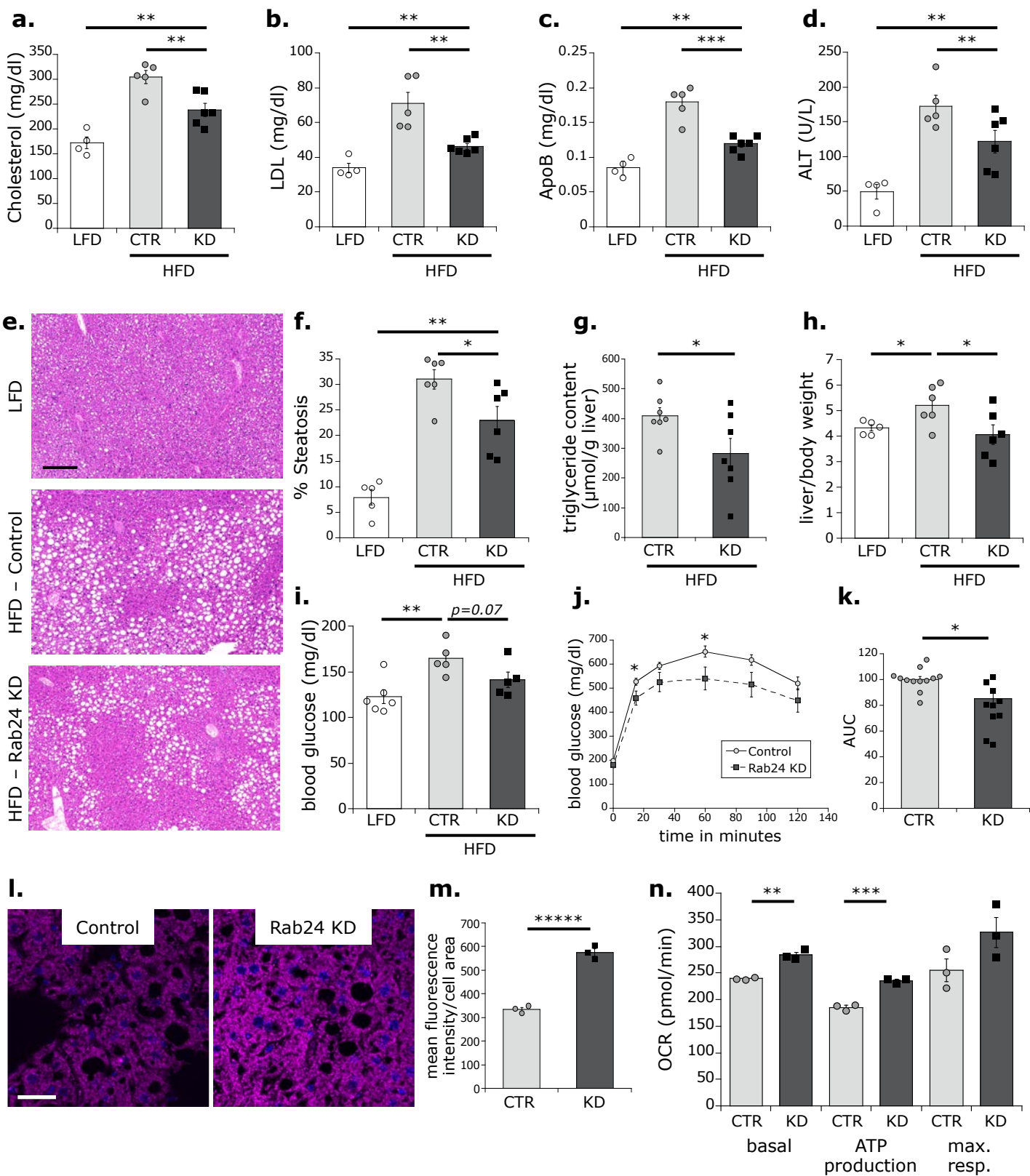


Figure 7

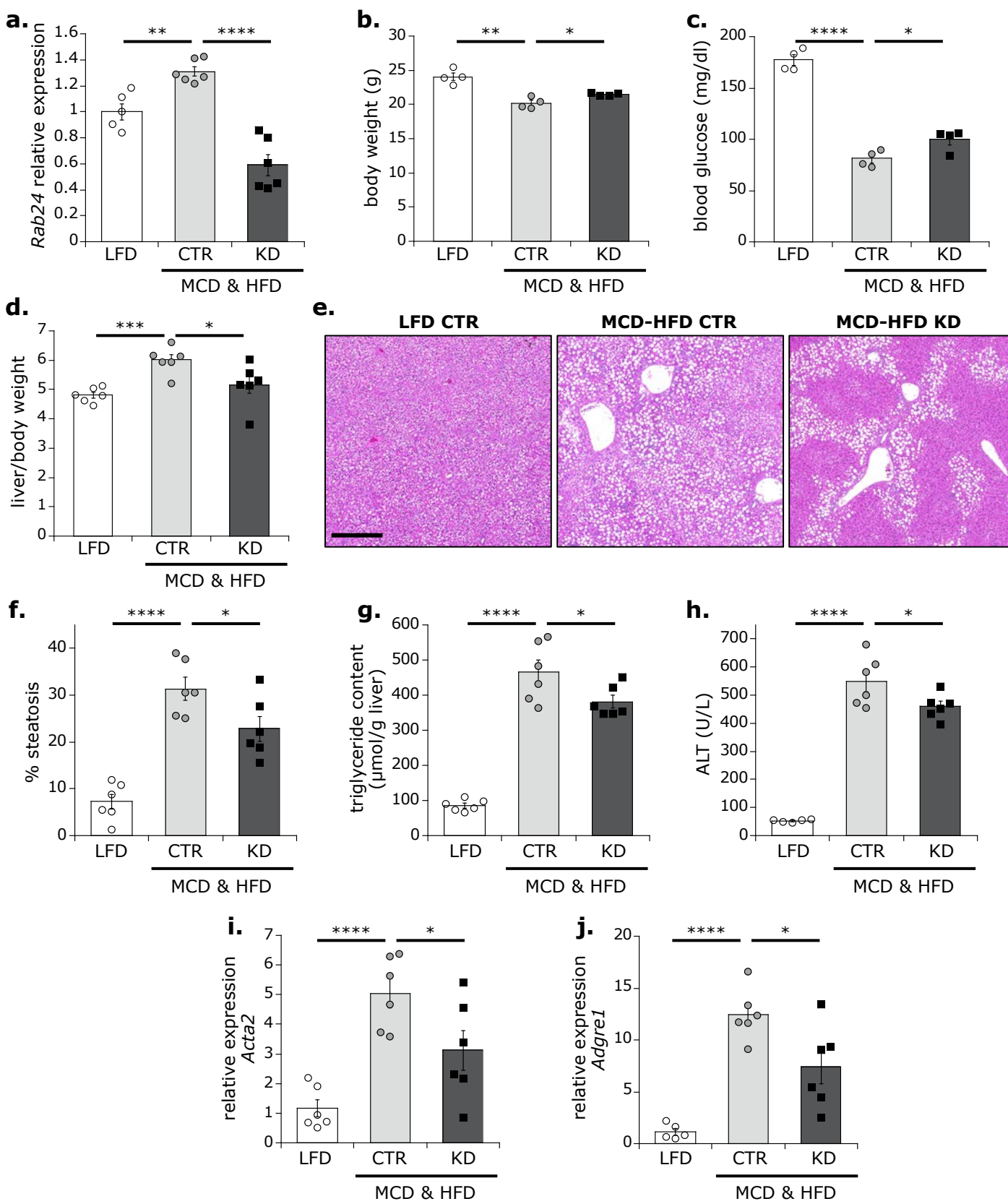
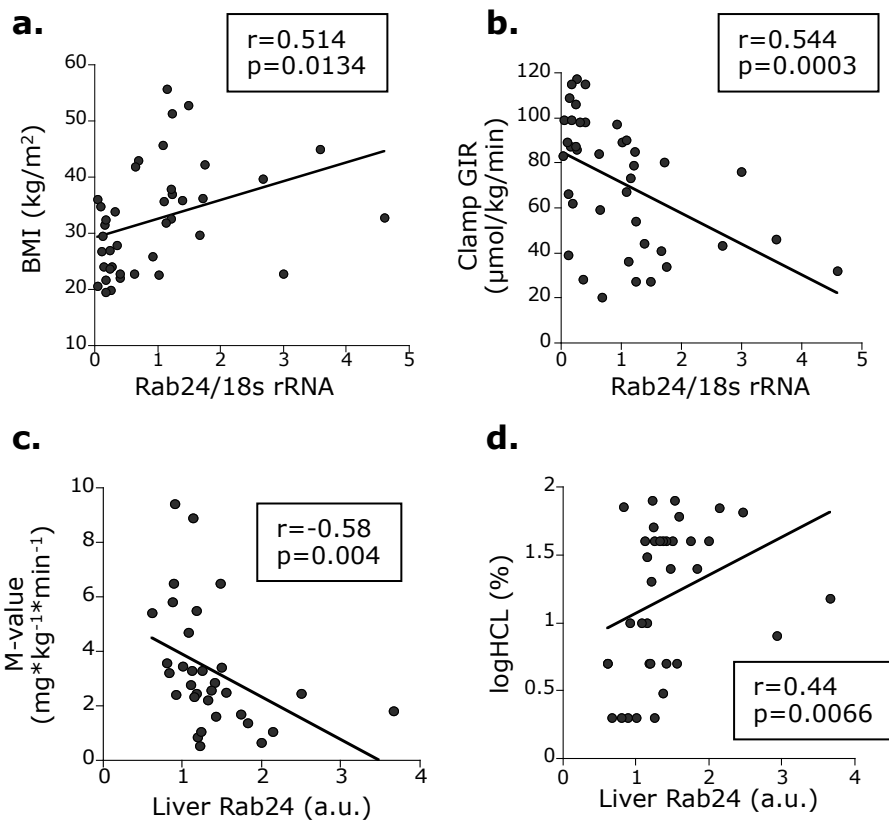
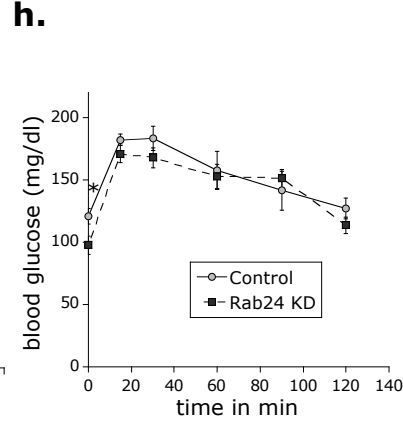
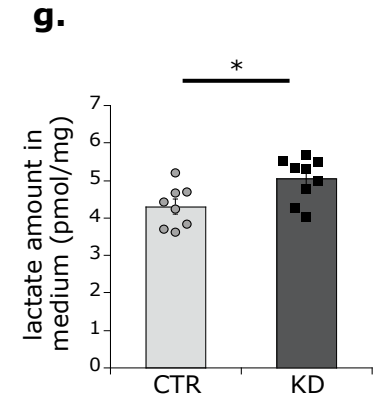
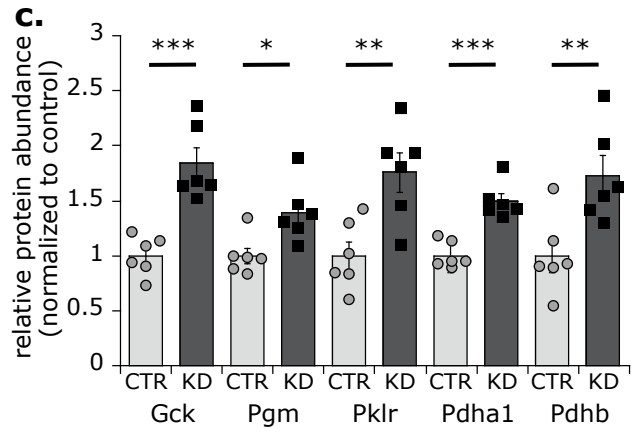
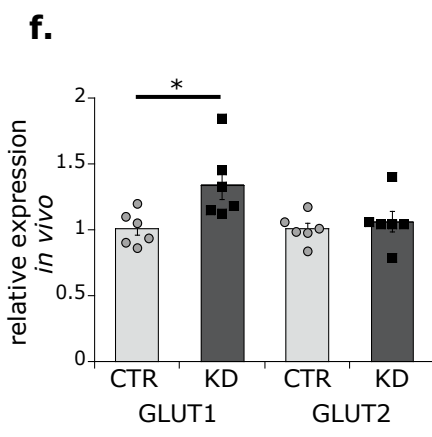
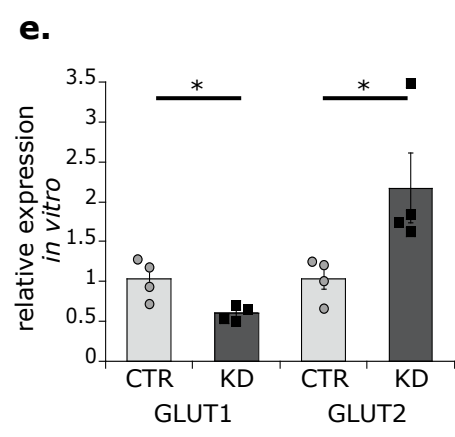
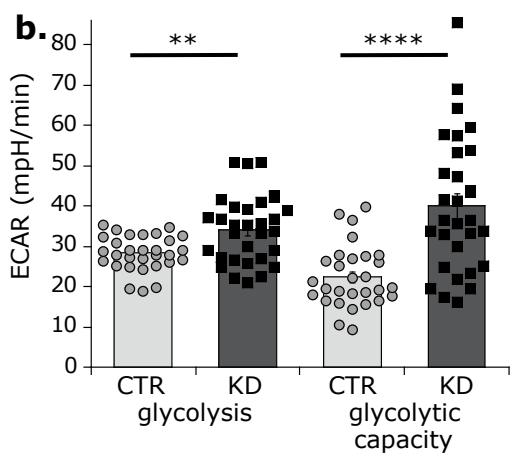
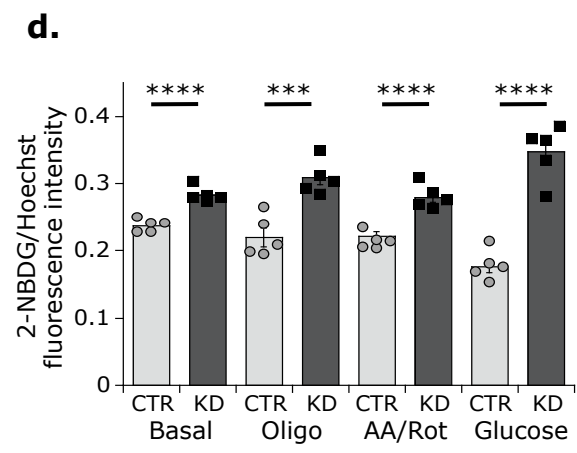
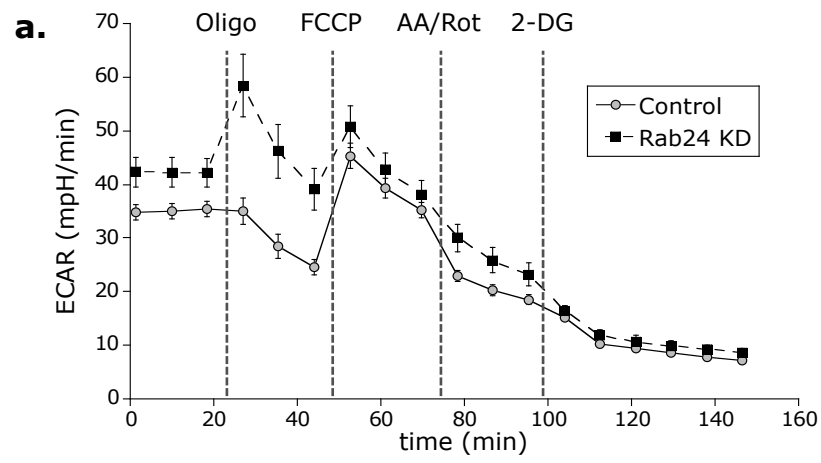
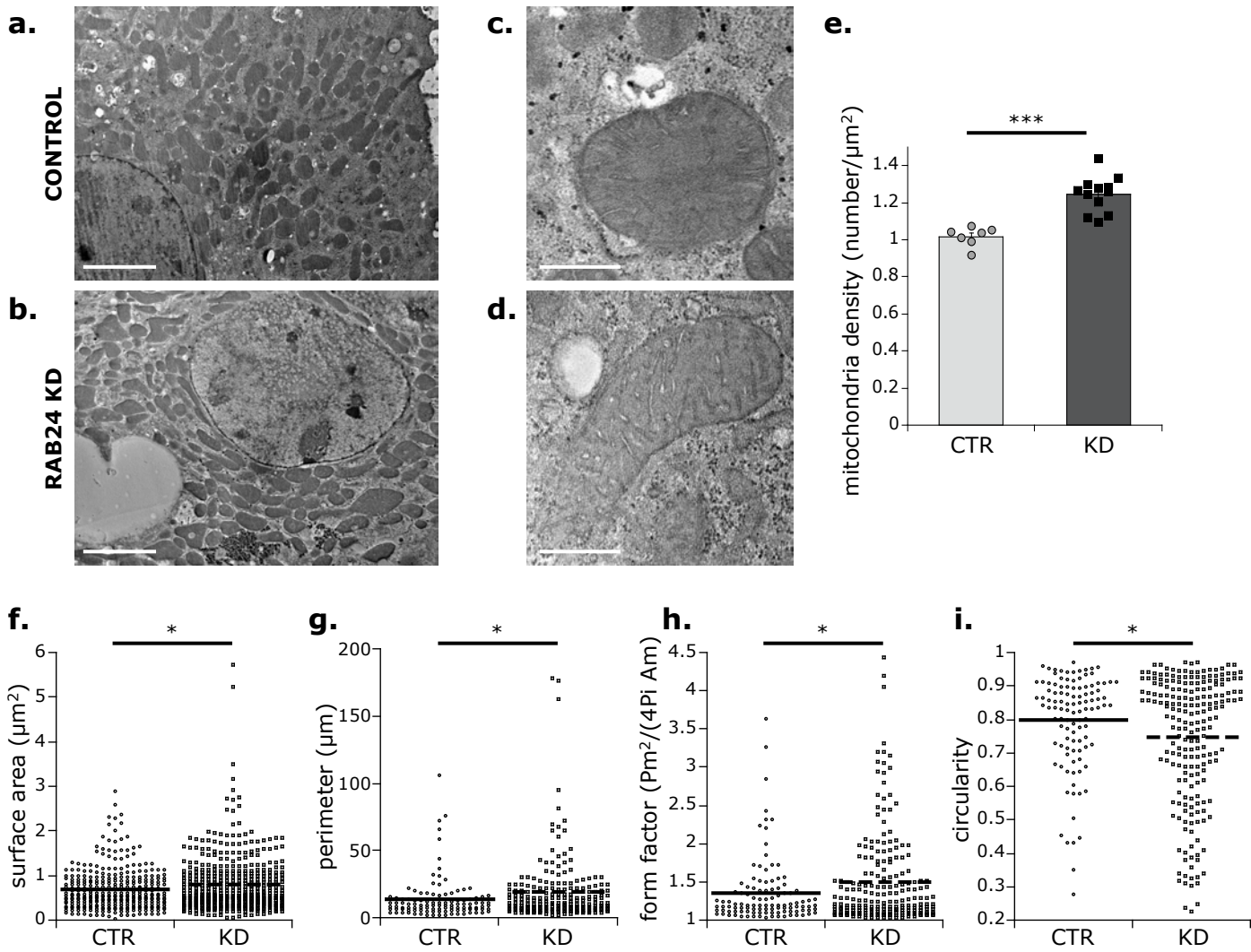
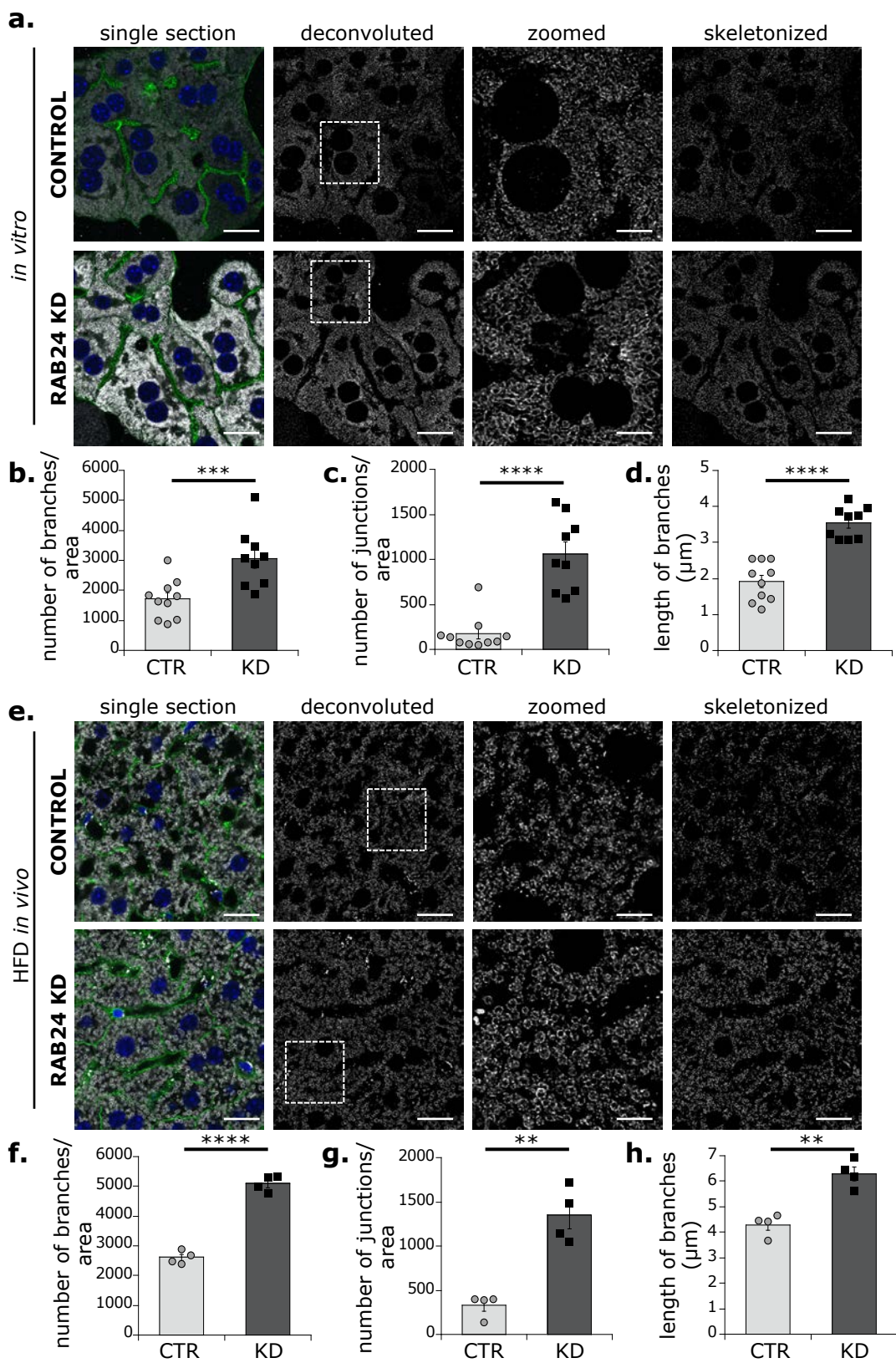


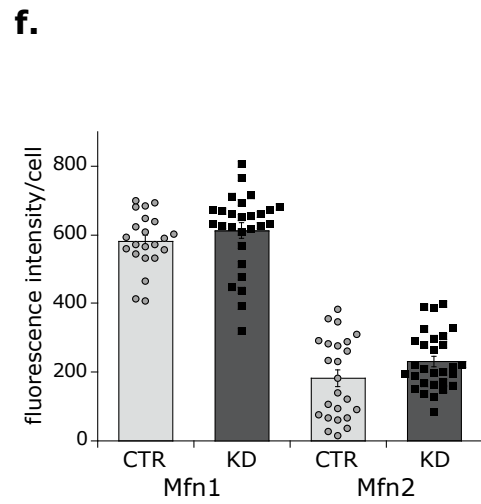
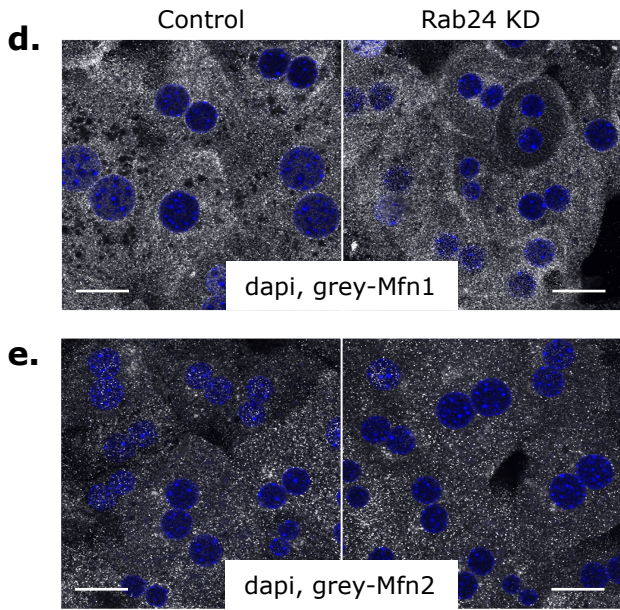
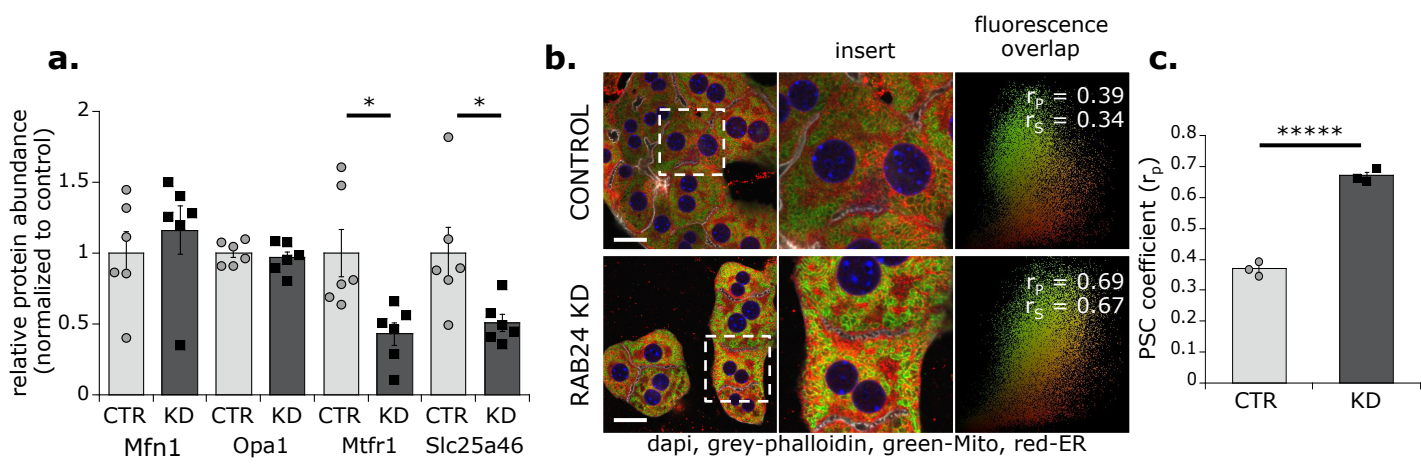
Figure 8

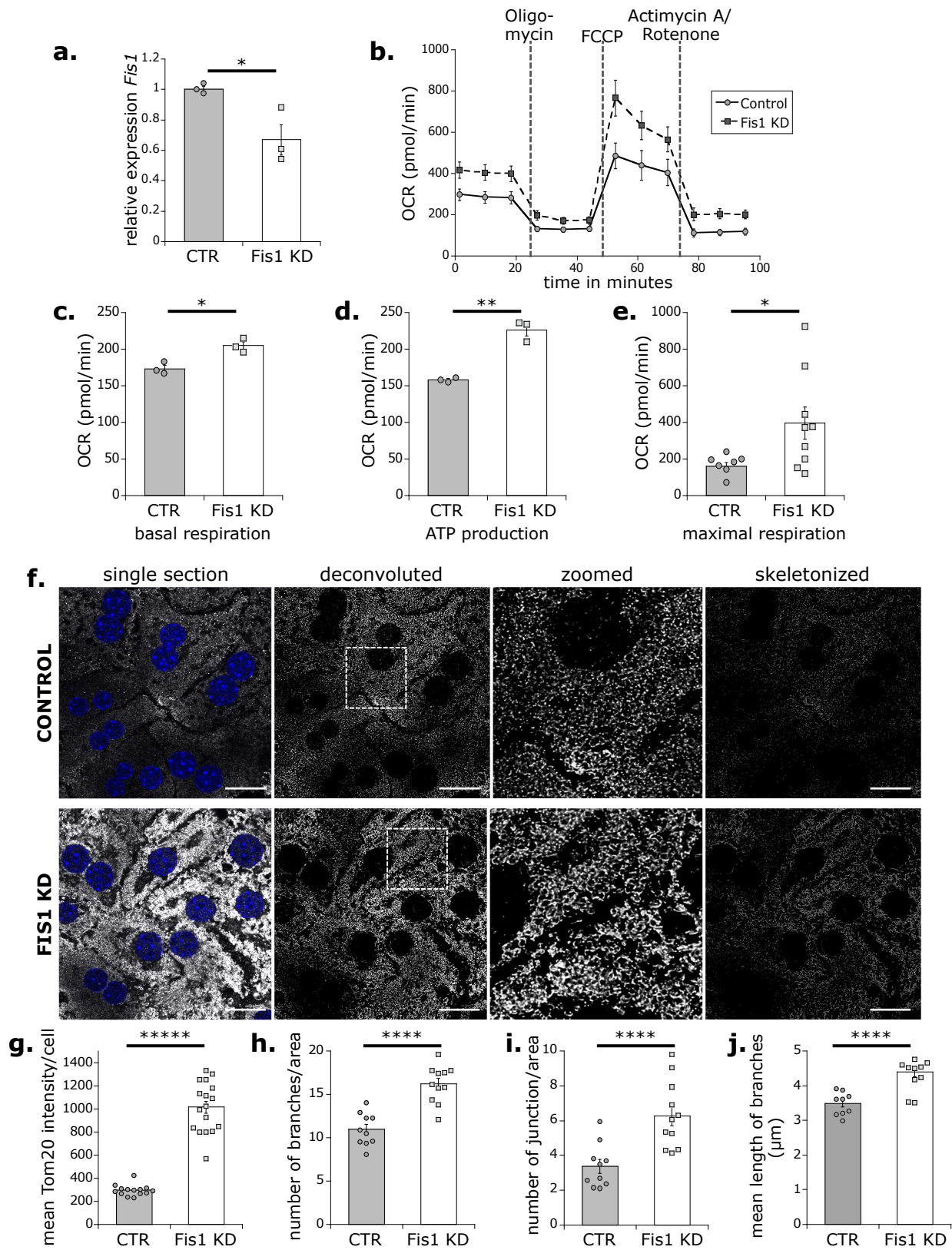


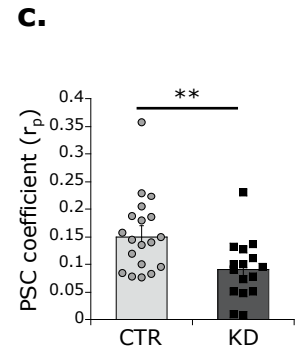
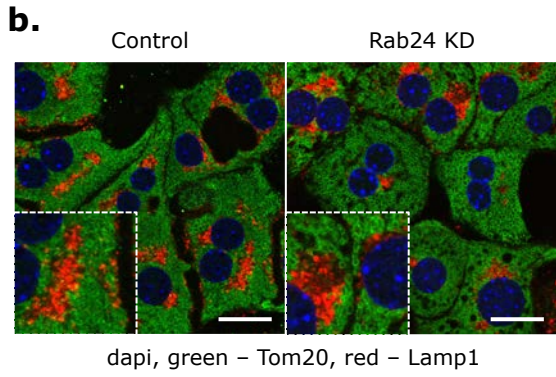
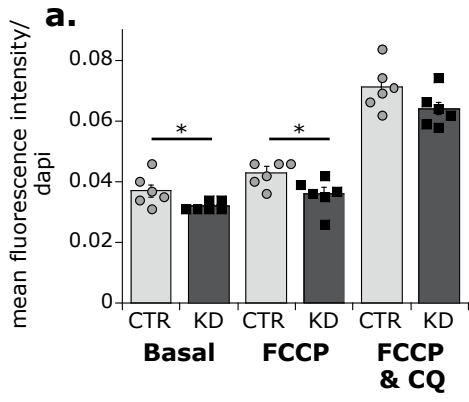


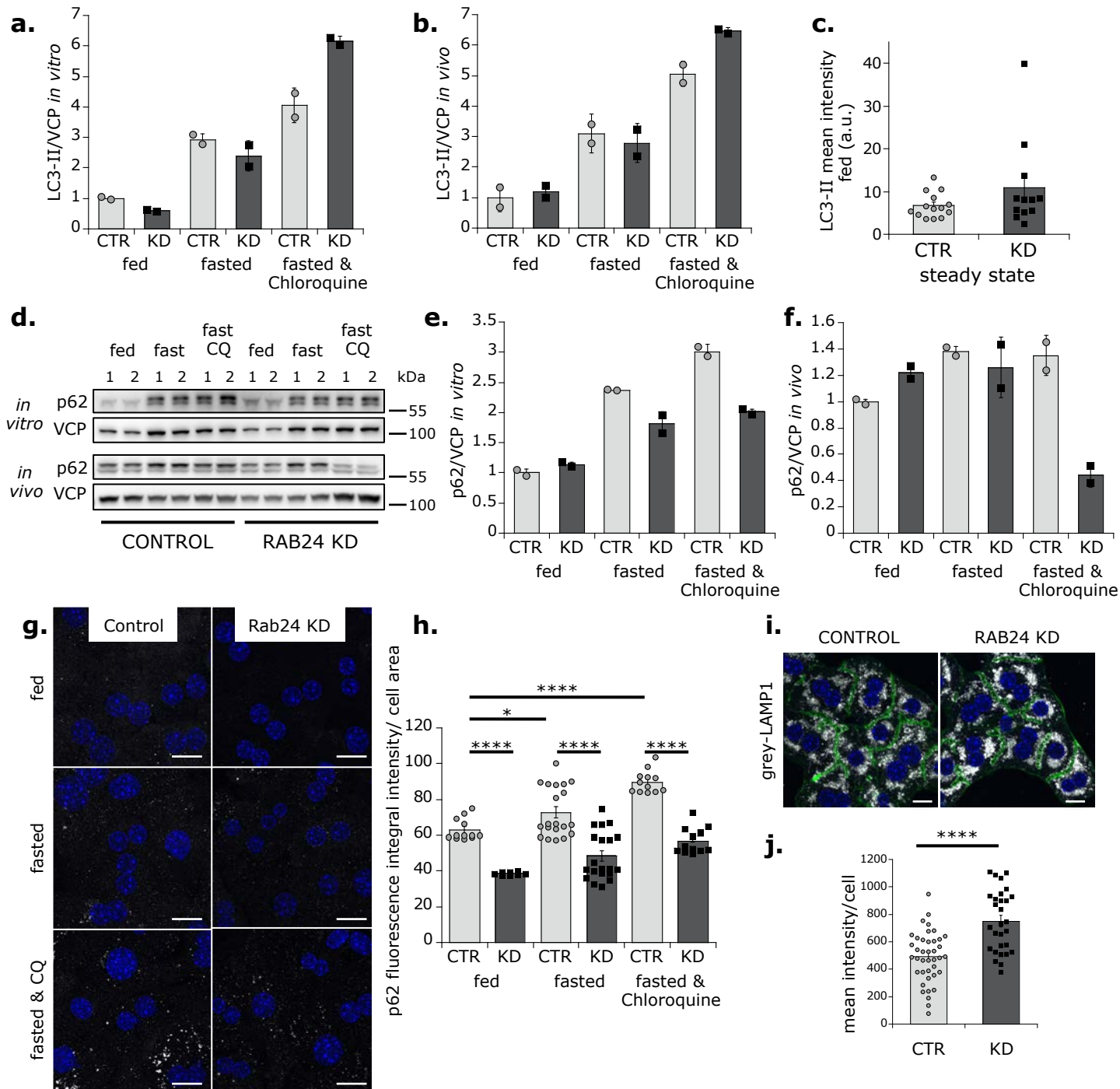


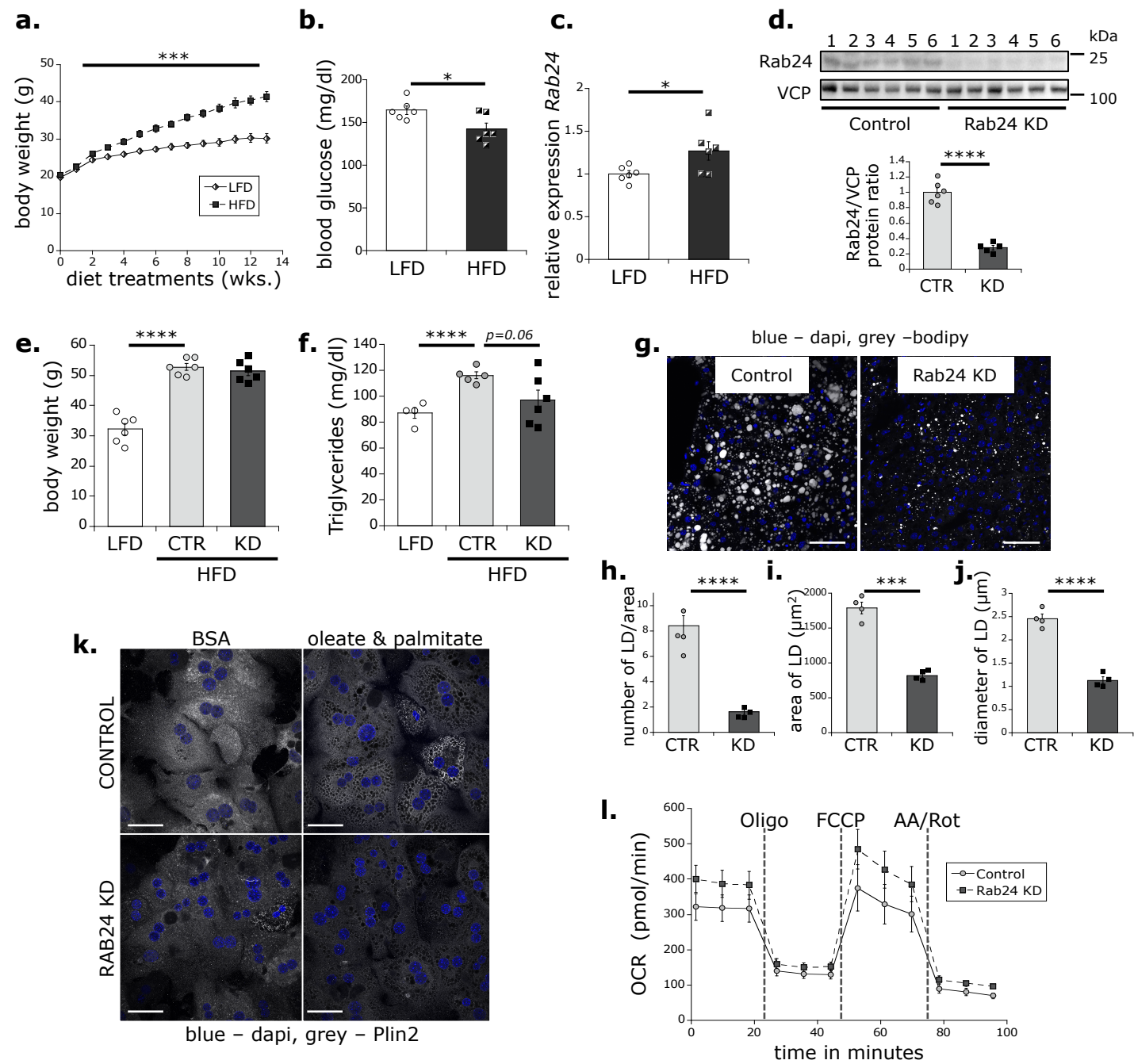


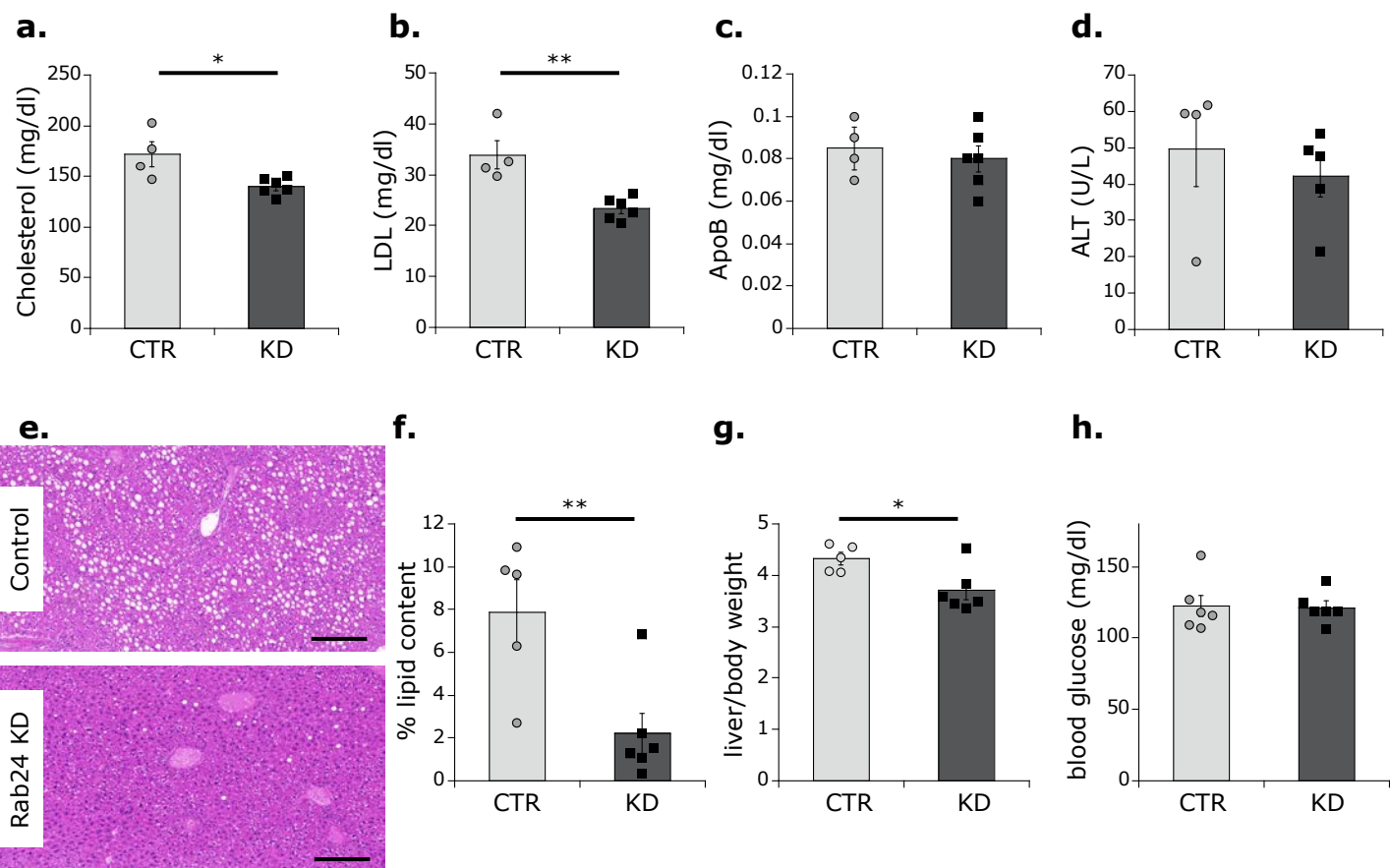


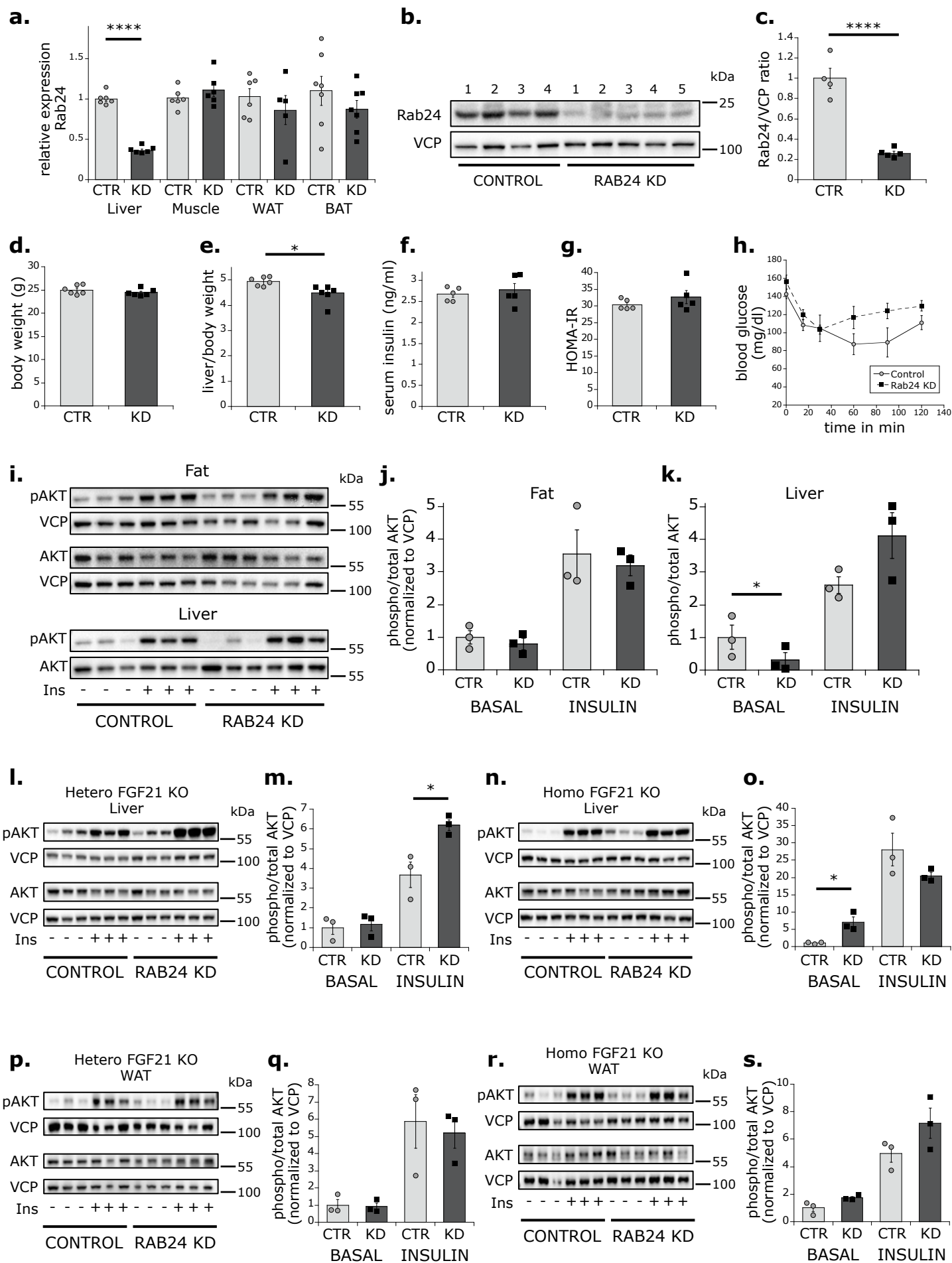




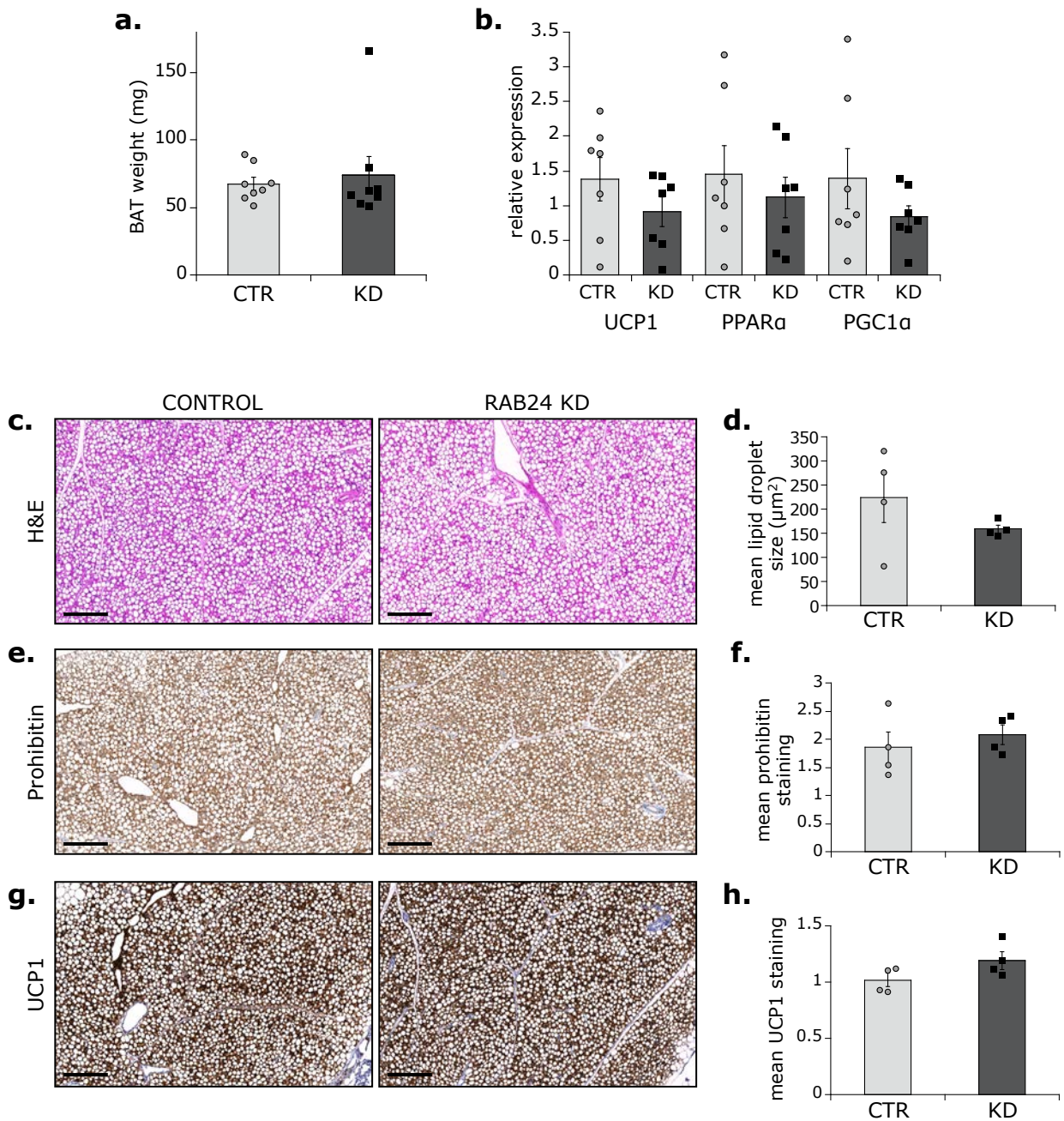




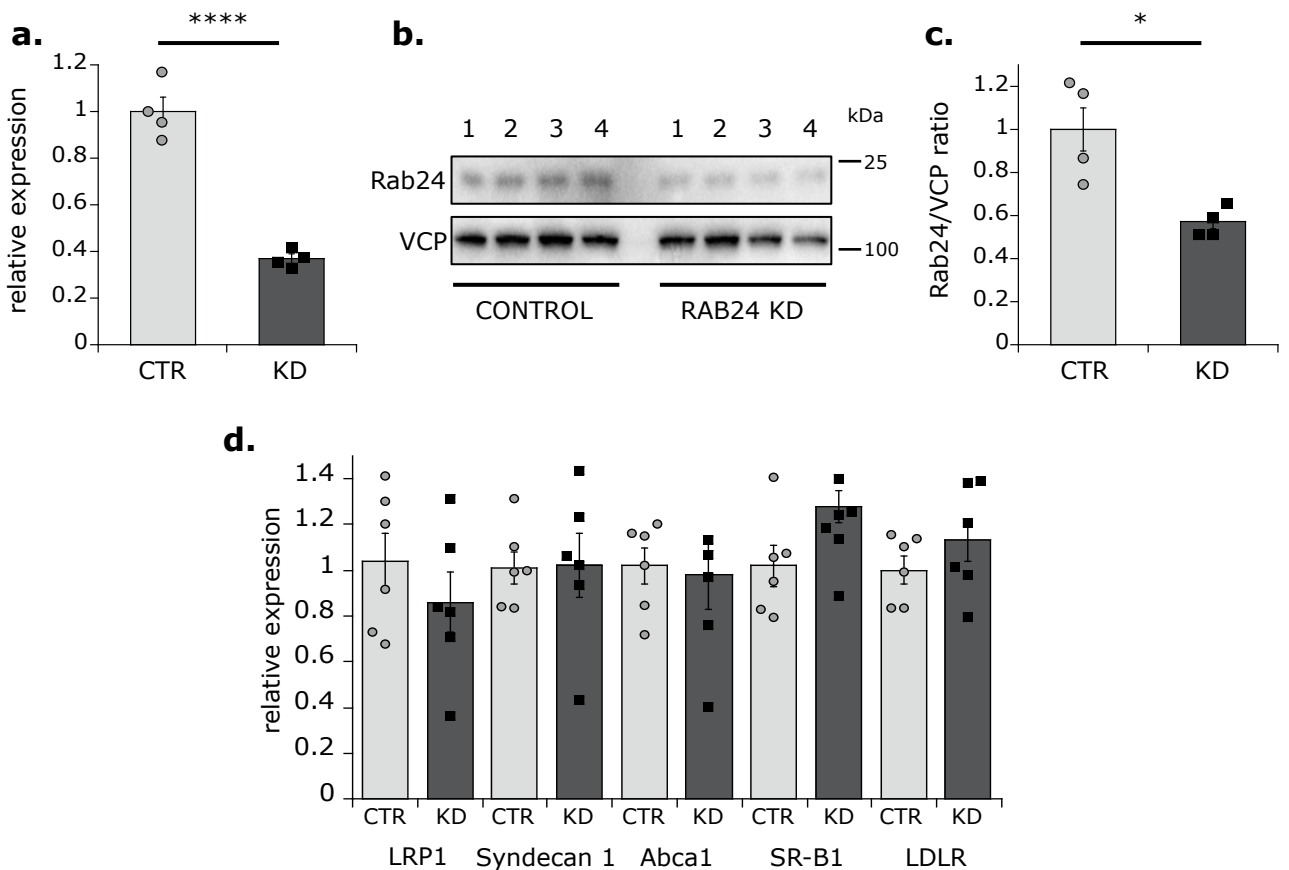




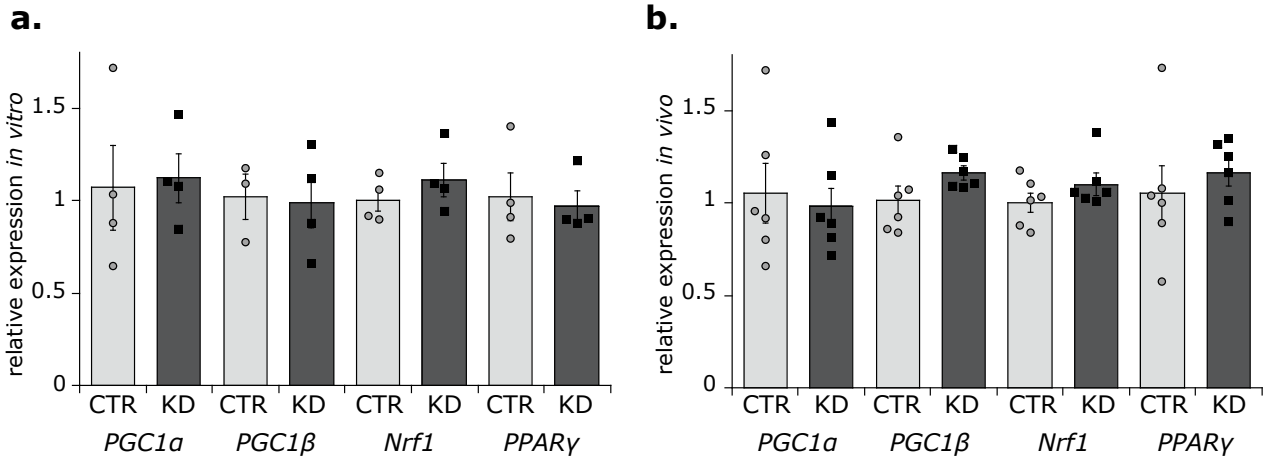
**Supplementary Fig. 1:** (a) Relative expression of *Rab24* in liver, muscle, WAT and BAT after RNAi treatment. N=6 for liver and muscle, N=6 (CTR) and N=5 (KD) for WAT, N=7 animals per condition for BAT. (b) Western blot analysis of liver lysates from control and Rab24KD mice and quantification thereof in (c). N=4 (CTR) and N=5 (KD) animals per condition. The experiment was repeated 10 times with similar results. (d) Body weight and (e) liver to body weight ratio after 6 days of Rab24KD. N=6 animals per condition (d, e). (f) Serum insulin, (g) HOMA-IR and (h) ipITT (0.75U/kg) of control and Rab24KD mice after RNAi treatment after 6 h of starvation on day 5 of KD. N=5 animals per condition (f-h). (i) Representative Western blots for Akt in fat and liver of insulin injected mice (0.75U/kg, 7 min) after 6 h fasting and quantification thereof in (j, k). The experiment was done twice with similar results. Western blots for Akt in liver of insulin-injected heterozygous (l) and homozygous (n) FGF21 KO mice (0.75U/kg, 7 min) after 6 h fasting and quantification thereof in (m) and (o), respectively. Representative Western blots for Akt in WAT of insulin-injected heterozygous (p) and homozygous (r) FGF21 KO mice (0.75U/kg, 7 min) after 6 h fasting and quantification thereof in (q) and (s), respectively. All treated with control (CTR) and Rab24 (KD) LNPs (0.5 mg/kg) (N=3 animals per condition). (mean+/-SEM) \*P<0.05, \*\*\*\*P<0.0001 by two-tailed unpaired Student's t-test. Only data that reached statistical significance are indicated.



**Supplementary Fig. 2:** (a) Brown adipose tissue (BAT) weight in heterozygous FGF21 KO mice. N=8 animals per condition. (b) Relative expression of browning markers in BAT upon control and Rab24KD. N=7 animals per condition. (c) H&E, (e) prohibitin and (g) UCP1 stainings of liver sections from control and Rab24KD mice and quantification thereof in (d), (f) and (h), respectively. Scale bar 200  $\mu$ m. The images are representative of four independent biological samples, which give rise to the quantifications in d, f and h. All measured after 5 days of LNP injection (0.5 mg/kg) and 6 h starvation. (mean  $\pm$  SEM). None of the weight, genes or markers were significantly changed based on a two-tailed paired Student's *t*-test.



**Supplementary Fig. 3:** (a) Relative expression of *Rab24* in primary hepatocytes after 3 days of RNAi (40 nM). (b) Western blot after KD and quantification thereof in (c). 12 wells pooled into N=4 replicates per condition. The experiment was repeated 10 times with similar results. (d) Relative expression of cholesterol transporters *LRP1*, *Syndecan2*, *Abca1*, *SR-B1* and *LDLR* in the liver after control (CTR) and Rab24 (KD) LNPs (0.5 mg/kg) (N=6 animals per condition, except N=5 for *Abca1*(KD)). (mean $\pm$ SEM) \*P<0.05, \*\*\*\*P<0.0001 by two-tailed unpaired Student's t-test. Only data that reached statistical significance are indicated.



**Supplementary Fig. 4:** Relative expression of mitochondria biogenesis markers *in vitro* (a) and *in vivo* (b) after Rab24KD. All mice treated with control (CTR) and Rab24 (KD) LNPs (0.5 mg/kg) (N=4 animals per condition, except N=3 for *PGC1β* (KD)). *In vitro* measured after 3 days of RNAi (40 nM) in primary hepatocytes (mean +/- SEM). 12 wells pooled into N=6 replicates per condition. None of the genes were significantly changed based on a two-tailed paired Student's *t*-test.

Table S3: Primers for RT-PCR

Symbol	Accession number	Name	Forward primer	Reverse primer
Rab24	NM_009000	RAB24, member RAS oncogene family	CATCCAGCAAGA-CAGGCCAAAG	GCTATGATAC-CGTTCTTGACCAG
FGF21	NM_020013	fibroblast growth factor 21	GTGTCAAA-GCCTCTAGGTTTCTT	GGTACACATT-GTAACCGTCCTC
Fis1	NM_001163243	fission, mitochondrial 1	CAAAGAG-GAACAGCGGGACT	ACAGCCCTCG-CACATACTTT
Gck	NM_001287386	glucokinase	TGAGCCG-GATGCAGAAGGA	CTCCCAGGTCTAAGGAGAGAAA
Pklr	NM_001099779	pyruvate kinase liver and red blood cell	TCAAGGCAGGGATG AACATTG	CACGGGTCTG-TAGCTGAGTG
Ppargc1a	NM_008904	Peroxisome proliferative activated receptor, gamma, coactivator 1 alpha	GAAGTGGTG-TAGCGACCAATC	AATGAGGG-CAATCCGTCTTCA
Ppargc1b	NM_001364996	Peroxisome proliferative activated receptor, gamma, coactivator 1 beta	GGGAAAAGGCCATC GGTGAA	TCACCGAACAC-CTCAAAGCG
Nrf1	NM_001164226	nuclear respiratory factor 1	ACAAACTCAGGCCA CCACCA	TGTACCAACCTG-GATGAGCGA
PPARG	NM_001127330	peroxisome proliferator activated receptor gamma	TGTGGGGATAAA-GCATCAGGC	CCGGCAGTTAA-GATCACACCTAT
Sdc1	NM_011519	Syndecan 1	GGAGAGGGCTCTG-GAGAACAAG	AATGACAC-CTCCCAGCACTTCC
LRP1	NM_008512	Low density lipoprotein receptor-related protein 1	CGAGAGCCTTT-GTGCTGGATGA	CGGATGTCCTTCTCAATGAGGG
SR-B1	NM_001205082	Scavenger receptor class B type 1	TTTGGAGTGGTAG-TAAAAAGGGC	TGACATCAGGGACTCAGAGTAG
LDLR	NM_010700	low density lipoprotein receptor	CAAGGTGTGCGACT CCGCCC	GGTCCACCAACCG-GAAGCCG
Abca1	NM_013454	ATP-binding cassette, sub-family A (ABC1), member 1	AAAACCGCAGA-CATCCTTCAG	CATAC-AC-CGAAACTCGTTCACC
Glut1	NM_011400	solute carrier family 2 (facilitated glucose transporter), member 1	TCAACAC-GGCCTTCACTG	CACGATGCTCAGA-TAGGACATC
Glut2	NM_031197	solute carrier family 2 (facilitated glucose transporter), member 2	TGCTGCTGGA-TAAATTCGCCT	TCAGCAAC-CATGAACCAAGGGA
Acta2	NM_007392	actin, alpha 2, smooth muscle, aorta	TGCTGACAGAGGCCA CCACTGAA	CAGTTGTAC-GTCCAGAGGCATAG
Adgre1	NM_001355722	adhesion G protein-coupled receptor E1	CGTGTTGTTGGTGG-CACTGTGA	CCACATCAG-TGTTCCAGGAGAC

Gapdh	NM_001289726	Glyceraldehyde 3-phosphate dehydrogenase	CACTGAG-CATCTCCCTCACA	GTGGGTG-CAGCGAACTTTAT
Rplp0	NM_007475	ribosomal protein, large, P0	AGATTCGGGA-TATGCTGTTGGC	TCGGGTCCTAGAC-CAGTG TTC
h_RAB24	NM_001031677	RAB24, member RAS oncogene family	AGAG-GAGGGCTGCCAAATCT	TGGCCTGTCTT-GCTGGATGT
h_TBP	NM_001172085	TATA-box binding protein	ACGCCAGCTTCG-GAGAGTTC	CAAACCGCTTGG-GATTATATTCG
h_GAPDH	NM_001256799	Glyceraldehyde 3-phosphate dehydrogenase	TGGCAAATTC CATGGCAAATTC CATGGCACCG	ATCTCGCTCCTG-GAAGATGGTG
h_RPLP0	NM_001002	ribosomal protein lateral stalk subunit P0	TGCTGATGGGCAA-GAACACC	CGGA-TATGAGGCAGCAG-TTCTC